



UNIVERSITY OF LEEDS

This is a repository copy of *Metasomatic reactions triggered by localized and dynamically evolving fluid flux record multistage intrusion history: An example from the syntectonic Caçapava do Sul Granitic Complex, Southern Brazil*.

White Rose Research Online URL for this paper:

<https://eprints.whiterose.ac.uk/196801/>

Version: Accepted Version

Article:

Hoerlle, GS, Remus, MVD, Müller, T et al. (3 more authors) (2023) Metasomatic reactions triggered by localized and dynamically evolving fluid flux record multistage intrusion history: An example from the syntectonic Caçapava do Sul Granitic Complex, Southern Brazil. *Lithos*, 442-443. 107103. ISSN 0024-4937

<https://doi.org/10.1016/j.lithos.2023.107103>

© 2023 Elsevier B.V. All rights reserved. This manuscript version is made available under the CC-BY-NC-ND 4.0 license <http://creativecommons.org/licenses/by-nc-nd/4.0/>.

Reuse

This article is distributed under the terms of the Creative Commons Attribution-NonCommercial-NoDerivs (CC BY-NC-ND) licence. This licence only allows you to download this work and share it with others as long as you credit the authors, but you can't change the article in any way or use it commercially. More information and the full terms of the licence here: <https://creativecommons.org/licenses/>

Takedown

If you consider content in White Rose Research Online to be in breach of UK law, please notify us by emailing eprints@whiterose.ac.uk including the URL of the record and the reason for the withdrawal request.



eprints@whiterose.ac.uk
<https://eprints.whiterose.ac.uk/>

[Click here to view linked References](#)

1. INTRODUCTION

Fluid flow is a fundamental process governing the distribution of elements in many geological settings, providing a much more efficient transport mechanism than solid state diffusion. Addition and removal of chemical components and modifications of mineral and bulk composition of rocks are directly linked to metasomatic processes, typically recorded by the dissolution of pre-existing minerals and precipitation of new phases (e.g., Nabelek et al., 2013; Engvik et al., 2018). However, fluid flow often occurs in heterogeneous and anisotropic media, in which case the fluid flow is structurally and/or lithologically controlled resulting in localized metasomatic domains that record the characteristics of fluid-rock interaction over time. Deciphering the spatial and temporal evolution of fluid-mediated rock alteration is crucial to understand complex processes in natural settings. Detailed studies of the zones of metasomatic reactions in terms of reaction textures and spatial distribution hold a wealth of information regarding the conditions at which fluid-rock interaction occurred.

Carbonate rocks and their metamorphic equivalents are typically highly reactive when exposed to externally derived fluids or changing metamorphic conditions (e.g., Bucher-Nurminen, 1981; Müller et al., 2004; Bégué et al., 2020). In particular, crystallizing plutons in contact with carbonate rocks constitute important heat and fluid sources causing metamorphism and skarn formation. Therefore, skarns are useful to obtain information on metasomatic interaction and contact metamorphism conditions. In this paper we use the term skarn for metasomatic rocks made of Ca–Fe–Mg–(Mn)-silicates and carbonates often with sequences of compositional zones and bands, formed by the interaction of a carbonate and a silicate system in mutual contact. If the carbonate part is dominantly made of dolomite, the metasomatic rocks are described as magnesian skarns. This variety of skarn typically contains forsterite, diopside, phlogopite, spinel and/or humites whereas

26 some minerals such as quartz and/or calcite are present in almost all skarns (Meinert et
27 al., 2005).

28 In general, there is a causal relationship between the sequence of emplacement,
29 crystallization, alteration, and cooling of an intrusion and the corresponding spatial and
30 temporal evolution during prograde and retrograde skarn formation (Brown et al., 1985;
31 Meinert et al., 2005). Detailed knowledge on the mechanisms, rates, and timing of the
32 emplacement of plutonic bodies remains elusive but significantly impacts our
33 understanding of the processes forming the associated metasomatic complexes. For
34 example, several authors proposed that plutons ascend as large diapirs (e.g., Buddington,
35 1959; Miller & Paterson, 1999) whereas other authors consider this process as slow and
36 inefficient (e.g., Clemens and Mawer, 1992; Petford et al., 2000). Other authors suggest
37 that large igneous magmatic bodies are formed by the incremental supply of magma
38 through dyke- and sill-like structures that can build up a magmatic body over millions of
39 years (e.g., Petford et al., 2000; Coleman et al., 2004). However, the recognition of
40 incrementally assembled plutons recorded in the granitic rocks can be problematic
41 because temperature remains nearly homogeneous for a long time potentially obscuring
42 pristine contacts between individual increments (Bartley et al., 2008). Yet, magmatic
43 pulses with quiet intervals can last for tens of millions of years (i.e., protracted magmatism)
44 and result in overprinted granitic batholiths (e.g., He et al., 2018; Tichomirowa et al.,
45 2019). While the diapir, incremental and protracted models are conceptually plausible,
46 they are characterized by fundamentally different cooling and fluid infiltration histories.
47 Therefore, studying in detail the metasomatic fingerprint of the interaction of magmatic
48 fluids with host rocks offers the potential to reveal the detailed intrusion and infiltration
49 history of a complex plutonic body.

50 In this contribution, we combine field relations, petrology of metasomatic rocks and
51 LA-ICP-MS U-Pb dating of zircon, titanite and apatite of igneous apophyses of the

Neoproterozoic Caçapava do Sul Granitic Complex (CSGC) to determine the intrusion, deformation, and fluid infiltration history of the complex. The igneous complex intruded into the dolomitic marbles of the Passo Feio Metamorphic Complex (PFMC) on the eastern border of the São Gabriel Terrane, southern Brazil (Fig. 1a). The emplacement of the granitic complex resulted in a metasomatic system recorded by the formation of skarns and hydrothermal veins. The observations and geochronological data are successfully explained by a model of localized and dynamically evolving fluid-rock interaction that provide a full record of the intrusion history of the granitic complex confirming a protracted growth of the magmatic body.

2. GEOLOGICAL BACKGROUND

The Passo Feio Metamorphic Complex (PFMC) and the Caçapava do Sul Granitic Complex (CSGC) are located at the eastern border of the São Gabriel Terrane (SGT), which itself belongs to the Dom Feliciano Belt (DFB) (Figs. 1a-b). The Dom Feliciano Belt represents the southern portion of the Mantiqueira Province, i.e., the Neoproterozoic NE-SW orogenic system that extends from north-eastern Brazil to the south of Uruguay. The São Gabriel Terrane comprises a Neoproterozoic (920-680 Ma) juvenile magmatic arc association developed during the collision of the Kalahari and Rio de La Plata cratons (Fernandes et al., 1992; Hartmann et al., 2000; Saalman et al., 2011). The terrane is composed of metavolcanic-sedimentary supracrustal sequences that were metamorphosed under amphibolite facies conditions and subsequently intruded by juvenile calc-alkaline magmas, now present as orthogneisses, ophiolites and mafic-ultramafic complexes (Remus et al., 1993; Babinski et al., 1996; Hartmann et al., 2000; Hartmann et al., 2011). Additionally, the São Gabriel Terrane hosts several Neoproterozoic granitic intrusions (e.g., Caçapava do Sul Granitic Complex) and is partially covered by post-collisional volcano-sedimentary sequences.

2.1. Passo Feio Metamorphic Complex

The Passo Feio Metamorphic Complex is in the eastern border of the São Gabriel Terrane and consists of a supracrustal association of metapelite, amphibolite, marble, calc-silicate and metavolcanic rocks that were intruded by the Caçapava do Sul Granitic Complex (Bitencourt, 1983; Hartmann et al., 1990; Remus et al., 2000) in addition to sheeted carbonatite intrusions (Cerva-Alves et al., 2017).

The metamorphic events that formed the Passo Feio Complex have been subject to controversial discussions. While there is a consensus that the complex records at least two metamorphic events displaying an increasing metamorphic grade towards the granitic batholith, contrasting ideas have been proposed regarding the thermal effect of the intrusion on the metamorphic record. Some authors described hornblende-hornfels and pyroxene-hornblende facies rocks surrounding the granite up to a few hundreds of meters from the contact, which were gradually followed by albite-epidote-hornfels and greenschist facies rocks further from the contact based on extensive field mapping of the area (e.g., Silva-Filho & Matsdorf, 1987; Bortolotto, 1988). These authors interpreted the observed distribution of mineral assemblages to be the result of a primary regional metamorphic event ranging from greenschist to amphibolite facies, followed by a second contact metamorphic event associated with the intrusion of the Caçapava do Sul Granitic Complex. In contrast, other authors interpret both metamorphic events as regional, with the first one reaching amphibolite facies (staurolite zone) conditions and the second, synchronous to the intrusion, as a greenschist facies (chlorite zone) with thermal and infiltration effects restricted to the border of some apophyses (Bitencourt, 1983; Hartmann et al., 1990).

Zircon provenance studies in metapelites and schists revealed Archean, Paleoproterozoic and Neoproterozoic populations (3637 to 774 Ma) suggesting complex continental source areas (Remus et al., 2000; Lopes et al., 2015). C, O and Sr isotopic

103 compositions of the dolomitic marbles reveal carbonate deposition between 770 and 730
104 Ma (Goulart et al., 2013). LA-ICP-MS monazite dating yields a series of ages between 650
105 and 620 Ma, which were assigned to the first metamorphic event (Remus et al., 2010).
106 The second metamorphic event was then linked to the age of a granodiorite sill sample of
107 the CSGC of 562 ± 8 Ma based on SHRIMP U-Pb zircon dating (Remus et al., 2000).

108 **2.2. Caçapava do Sul Granitic Complex**

109 The Caçapava do Sul Granitic Complex exhibits a wide compositional range with
110 mostly granodiorite, monzogranite, leucogranite, minor diorite, tonalite and quartz-diorite of
111 metaluminous and calc-alkaline affinity (Sartori & Kawashita, 1985; Nardi & Bitencourt,
112 1989). The granitic batholith to the west of the dolomitic marbles outcrops over an area of
113 c. 233 km² forming a N-S elongated asymmetrical domal structure dipping at high angles
114 in the W and NW parts, at low angles in the E and SE parts, and sub-horizontally in the
115 central parts of the granitic body (Figs. 1b-c) (Sartori & Kawashita, 1985; Nardi &
116 Bitencourt, 1989). Pegmatite, aplitic dykes and quartz veins with pyrite and hematite occur
117 in the eastern border of the body near the dolomitic marbles.

118 Deformation is heterogeneous throughout the batholith ranging from undeformed
119 portions to highly foliated facies where boundaries between these facies vary from sharp
120 to diffuse. Foliation and banding are common and mostly marked by the preferred
121 orientation of biotite and amphibole, as well as elongate feldspar and quartz grains (Nardi
122 & Bitencourt, 1989). A N-S to NE-SW sub-horizontal mineral grain and aggregate lineation
123 is dominant in the granitic body and the foliation close to the boundary of the batholith is
124 mostly concordant to S₂ foliation of the surrounding metamorphic rocks (Nardi &
125 Bitencourt, 1989). Contrasting emplacement models were proposed: a diapir (Nardi &
126 Bitencourt, 1989), a sheet-like intrusion (Fragoso-César, 1991), a lens-shaped syntectonic
127 batholith (Fernandes et al., 1992) and an intrusion along a fault-bend-fold of a right lateral
128 strike-slip shear zone (Costa et al., 1995).

129 First attempts to date the Caçapava do Sul Granitic Complex were made through
130 K/Ar and Rb/Sr isochron dating, which resulted in ages ranging from 520 to 640 Ma
131 (Cordani et al., 1974; Sartori & Kawashita, 1985). Two different U-Pb SHRIMP zircon
132 studies were carried out on samples of a monzogranite and a granodiorite revealing a
133 complex distribution of zircon ages indicating significant amounts of lead loss and
134 reversely discordant ages (Leite et al., 1998; Remus et al., 2000). Two magmatic ages
135 were proposed based on SHRIMP zircon U-Pb analyses. The two studies reported two
136 similar concordant ages of 561 ± 6 Ma (MSWD=1.04; n=4; Leite et al., 1998) and 562 ± 8 Ma
137 (MSWD=0.56; n=18; Remus et al., 2000) and one age of 540 ± 11 Ma (MSWD=0.89; n=3;
138 Leite et al., 1998). The younger age of c. 540 Ma was re-interpreted as the result of
139 common Pb loss of older zircons (Remus et al., 2000). Inherited Paleoproterozoic zircon
140 populations with ages ranging from 1.7 to 2.4 Ga were reported in both studies. Large
141 variations in initial $^{87}\text{Sr}/^{86}\text{Sr}$ and ϵNd values, lead isotopes and zircon ages also suggest
142 that the CSGC had a complex and heterogeneous crustal source of variable composition
143 and age (Babinski et al., 1996; Remus et al., 2000).

144 3. SAMPLING AND METHODS

145 Collection of field data and sampling focused on the Caçapava do Sul marble
146 quarries due to the extensive exposure of marbles, igneous apophyses and metasomatic
147 rocks (skarns and hydrothermal veins) providing the opportunity to sample the best
148 sections for the study of igneous and carbonate rock interaction in the region. Sample
149 collection was made throughout the area aiming at obtaining representative samples of the
150 different igneous components and skarns displaying their various degrees of deformation,
151 spatial relationships, and retrograde alteration. Petrographic analyses were made using a
152 LEICA DM4500 optical microscope and a LEICA S6D Greenough stereo microscope to
153 identify major constituent minerals and textures. Zircon, apatite and titanite grain
154 concentrates were prepared at the Sample Preparation Laboratory at the Geosciences

155 Institute of UFRGS (IGEO/UFRGS) using conventional jaw crusher, milling, manual
156 panning, magnetic-Frantz isodynamic separator and heavy liquids separation. The grains
157 were handpicked under a binocular microscope and mounted on epoxy disks. U-Pb laser-
158 ablation inductively coupled plasma mass spectrometry (LA-ICP-MS) analyses of zircon,
159 apatite and titanite samples were performed at the Isotopic Geochemistry Laboratory,
160 Federal University of Ouro Preto (IGL-UFOP). Back-scattered electron (BSE) and
161 cathodoluminescence (CL) images were obtained with a JEOL JSM-6610LV and a JEOL
162 6510 scanning electron microscopes at IGEO-UFRGS and DEGEO-UFOP, respectively, to
163 identify internal structures of the crystals. The LA-ICP-MS analyses were performed using
164 a ThermoScientific Element 2 sector field (SF) ICP-MS coupled to a CETAC LSX-213 G2+
165 laser system. Spot sizes were set at 30 μm for zircon and 50 μm for titanite and apatite.
166 Zircon analyses calibration included GJ-1 (Jackson et al., 2004) with the additional
167 Plešovice (Sláma et al., 2008) and Blue Berry (Santos et al., 2017) zircon standards. For
168 titanite and apatite reference materials, BLR-1 (Aleinikoff et al., 2007) and KHAN (Kinny et
169 al., 1994) were used for the titanite while 401 (Thompson et al., 2016) and Madagascar
170 (Thomson et al., 2012) were used for the apatite. Glitter Data Reduction Software for laser
171 ablation was used to reduce data (Van Achterberg et al., 2001). Calculated ages and
172 concordia diagrams were done using Isoplot 3.0 (Ludwig, 2003) and errors are reported at
173 the 2σ level. The calculated titanite and apatite ages are the lower intercept of anchored
174 regressions through the $^{207}\text{Pb}/^{206}\text{Pb}$ ratio of the crustal lead at the time of formation of the
175 titanite and apatite (i.e., Pbc), as defined by Stacey and Kramers (1975) on the Tera-
176 Wasserburg diagram. The anchoring ratios are based on the samples intercept age and
177 the zircon ages. T- XCO_2 and XCO_2 - μSiO_2 phase diagrams were calculated using PerpleX
178 (Connolly, 1990) using the dataset from Berman (1996) and equation of state for fluids
179 from Holland and Powell (2011). Abbreviations for the mineral names and their end-
180 members described in the text and figures are after Whitney and Evans (2010).

4. GENERAL FIELD RELATIONSHIPS

Dolomitic marbles are present in the eastern portion of the metamorphic complex and occur as lenticular bodies that are extensively intruded by tabular felsic and mafic apophyses of variable thickness and composition (Figs. 2a-d). They occur to the east of the main granitic body of the CSGC (i.e., the granitic batholith; Figs. 1b-c) with sharp and eastward dipping contact at low to medium angles ($\sim 10\text{-}30^\circ$). In this paper, we refer to the bedding of the marbles as S_0 and the metamorphic foliation developed during the first metamorphic event (regional amphibolite facies conditions) prior to the first magmatic intrusions as S_1 . Bedding (S_0) is generally difficult to decipher except where there is compositional change characterized by fine to medium grained metamorphic layers with talc and tremolite resulting in gray tones (Fig. 2f). The silicate content of the dolomitic marbles varies from 2% in massive white marbles up to 15% in banded gray layers. S_1 foliation is well developed and defined by elongated crystals of dolomite, dominantly parallel to bedding. The marbles and some of the apophyses (mainly mafic ones) form overturned to recumbent isoclinal folds with N-S to NE-SW fold axis that plunges at low angles mostly to the S-SW (Figs. 2a-e). The axial surfaces define the S_2 foliation. The average axial surface dips 20° to the east, locally varying to sub-horizontal or rarely dipping westward at low angles ($<15^\circ$). Ductile deformation prevails towards the contact with the granitic batholith (i.e., Dagoberto Barcelos quarry area (DB); Fig. 1b). Marbles with a platy aspect caused by the foliation and highlighted by an intercalation of low and high strain areas (Fig. 2f) prevail in the eastern portion of the metamorphic complex (i.e., Inducal quarry area (IN); Fig. 1b). Low strain areas are characterized by a grain size of a few millimetres ($\sim 2\text{ mm}$) and granular aspect with nearly equidimensional grains. In contrast, the high strain portions exhibit a range of grain sizes including 1-2 mm-sized porphyroclasts within a fine-grained matrix, elongate crystal shapes seen for larger grains and a closely spaced foliation (Fig. 2f).

207 Tabular felsic and mafic intrusions within the dolomitic marbles are well exposed in
208 the quarries. A group of mafic and felsic apophyses with small to moderate thickness (~0.1
209 to 1 m) intruded parallel to the S_1 foliation of the marbles and are folded during the
210 deformation event that produced the S_2 foliation (Figs. 2a-d). For simplification, this group
211 of thin and folded mafic-felsic apophyses are identified as A1. A1 mafic apophyses form
212 tabular bodies predominantly continuous for tens to hundreds of meters and concordant to
213 the S_1 foliation. A1 mafic apophysis-marble contacts vary from sharp to diffuse. A1
214 apophyses are often strongly foliated and marked by the preferred orientation of mafic
215 minerals. The observed foliation is parallel to sill orientation and to S_1 foliation of the
216 country rocks. There are no clear cross-cutting relationships between the A1 mafic and
217 felsic apophyses; instead, if they occur in the same outcrop, they are seen to form one
218 intrusive body with interlayered mafic and felsic bands with parallel boundaries (Figs. 2b-d;
219 6a). This suggests that these composite mafic-felsic sills formed contemporaneously from
220 A1 mafic and felsic magmas.

221 Thicker tabular felsic apophyses (> 2 m) intruded the marbles parallel or sub-
222 parallel to the S_2 foliation and are referred to in the following as A2. Given that the
223 orientation of A2 apophyses is parallel to the S_2 axial plane foliation and that A2
224 apophyses host mafic enclaves (Fig. 6b), likely from A1 apophyses, we consider A2
225 younger than A1. However, in some cases, distinguishing A2 and A1 felsic apophyses is
226 difficult. Main criteria used for distinguishing A1 and A2 felsic apophyses are thickness,
227 grain-size, and emplacement-host geometry. A1 felsic apophyses are thin (20-100 cm),
228 have fine to medium grain size and are commonly folded whereas A2 apophyses are
229 thicker (~ 2 to >10 m), have medium to coarse grain size and emplaced parallel to the S_2
230 axial plane foliation (Section 4.4.2). Contacts of A2 apophyses with the marbles are often
231 sharp and unreacted, although diopside and forsterite skarns are developed in the
232 dolomites at many of these contacts (Figs. 3a-b). A2 apophyses are mainly represented by

233 granodiorite, monzogranite and syenogranite intrusions, which correspond to the main
234 facies of the Caçapava do Sul Granitic Complex described in previous studies (e.g., Nardi
235 & Bitencourt, 1989). Late pegmatite bodies and leucogranites are associated with the A2
236 intrusions and occur as small portions within sills (Figs. 3b and 6b) or as irregular bodies
237 predominantly cutting A1 and A2 mafic and felsic apophyses (Fig. 6d).

238 The marbles were locally replaced by skarns that are found at the contacts or a few
239 meters away from A1 and A2 apophyses (Figs. 2d,g; 3a-d; 4a-c). Skarns at the lithological
240 contacts of A1 apophyses are asymmetric relative to the lithological boundaries, i.e., skarn
241 is not always developed at each lithological interface (Fig. 3c). Even along the same
242 apophysis-country rock interface, the skarn is discontinuous (Fig. 3a). There is no
243 preferred occurrence of skarns in the structurally upper or lower borders of the apophyses.
244 Skarn bodies are variable in thickness (5 – 100 cm) and texture (Figs. 3c-d). Thicknesses
245 are generally higher close to the apophysis-country rock contact and thin away from the
246 contact. No spatial relation between the contact type and thickness of the skarn was
247 identified. Nevertheless, skarns are more frequent at fold hinge zones or terminations of
248 the A1 mafic apophyses (Figs. 2d and 3c). Bodies of skarn commonly form parallel to the
249 pre-existing S₁ foliation (Fig. 3a). However, the skarns locally crosscut the S₁ regional
250 metamorphic foliation (Figs. 2g and 3a). Skarns are also seen to “follow” S₂ foliations and
251 form sigmoidal extension veins (Fig. 2g).

252 Skarns are divided into diopside and forsterite skarns. Diopside skarns consist of
253 coarse diopside grains with variable amounts of sulphides and tremolite + calcite whereas
254 forsterite skarns consist of two zones defined by the silicate present, i.e., forsterite and
255 phlogopite zones. The phlogopite zone, however, is difficult to recognize in the field due to
256 its macroscopic similarity to the dolomitic marbles. The skarns are frequently associated
257 with each other resulting in zoned skarns where the diopside zone typically occurs in the
258 center, bordered, or partly replaced by the forsterite and phlogopite zones (Figs. 3c-d; 4b-

c). The two skarn types occur either separately or combined. If combined, then the di-skarn is at the centre and the fo-skarn at the interface to the country rock (Figs. 3d and 4b-c). There is no systematic spatial difference in association with A1 and A2 for the two skarn types. Both skarn types are seen to forming extensional features with diopside skarn forming pinch-and-swell and boudin structures with clear shear fractures (e.g., Fig. 4a) while forsterite skarn show a lack of fractures but gentle pinch and swell structures (Figs. 3b; 4a). Less commonly and limited to the northernmost quarry (CL area in Fig. 1b), the carbonates host calcite-chlorite-sulphide veins and breccias that cut S_1 and S_2 foliation and are generally found a few to tens of meters from NW-SE subvertical faults (Figs. 5a-c).

5. PETROGRAPHY AND MICROSTRUCTURES

In this section, we describe the petrographic characteristics of igneous apophyses and skarns. Petrographic and geochemical characterization of the main facies of the granitic batholith can be found in previous studies (Sartori & Kawashita, 1985; Nardi & Bitencourt, 1989). Petrography and geochemistry of the dolomitic marbles were presented and discussed in Goulart et al. (2013).

5.1. A1 mafic and felsic apophyses

Even though the mafic intrusions show similar aspects in the field, mineral assemblages and microstructures reveal heterogeneity among A1 mafic apophyses. Typical mineral assemblages consist of amphibole + biotite + plagioclase \pm K-feldspar \pm quartz (Figs. 7a-d and 8d-f). Amphibole + biotite + plagioclase are present in all samples in variable proportions (Figs. 7a-d) whereas K-feldspar and quartz occur in some of the samples (Figs. 7a, 7c and 8d). Felsic minerals (quartz, plagioclase and K-feldspar) occur mostly in the groundmass. Amphiboles vary from subhedral short hornblende grains (Figs. 7c and 8d) to subhedral short to elongate actinolite (Figs. 7c and 8e-f) and less commonly subhedral to euhedral tremolite. In general, biotite occurs as discontinuous lenticular and often anastomosing aggregates (Figs. 7a-d and 8e-f). Biotite also occurs as inclusions in

coarse grained and equidimensional hornblende crystals that resembles phenocrysts. The foliation in these rocks is well defined by the preferred orientation of the actinolite and biotite (Figs. 7a-d). Biotite and amphibole occur as phenocrysts and in the groundmass. Some samples also show a subtle crenulation highlighted by shear bands defined by the biotite (Fig. 7b). Local chloritization of biotite occurs near fractures or micro shear zones (Fig. 7a). Titanite and apatite are common accessories. Titanite occur mostly within biotite aggregates and less commonly included in hornblende (Figs. 8a-d) whereas apatite is frequently found in the grain boundaries of actinolite and generally with the same preferred orientation as that of the amphiboles (Figs. 8b-c). Disseminated pyrite and chalcopyrite were identified in all A1 mafic apophyses in variable amounts; higher contents were observed in samples located up to tens of meters away from sub-vertical NW-SE trending faults that cut the A1 mafic apophyses in the northernmost quarry (CL area in Fig. 1b). In a few places, molybdenite was found disseminated in the A1 mafic apophyses.

A1 felsic apophyses are less common than A1 mafic apophyses and A2 felsic apophyses. In general, the A1 felsic apophyses comprise equigranular fine to medium grained (0.05 – 0.2 mm) rocks composed of K-feldspar, quartz, plagioclase, and biotite (Figs. 9a-b). Disseminated apatite and pyrite are common (Fig. 9b). Biotite occurs mainly along K-feldspar and quartz grain boundaries and its preferred orientation characterizes a subtle foliation in the A1 felsic apophyses (Figs. 9a-b).

5.2. A2 felsic apophyses

The A2 felsic apophyses comprise mostly granodiorite, monzogranite and less commonly syenogranite and pegmatite. Biotite and hornblende are the main mafic minerals and biotite-hornblende granodiorites represent the most common type of A2 felsic apophyses (Figs. 9c-d). Quartz, K-feldspar, and plagioclase occur in various proportions amongst different apophyses. Foliation in these rocks is characterized by the preferred orientation of biotite, amphibole, and K-feldspar phenocrysts (Fig. 6c). The grain size and

311 the amount and proportion of biotite and amphibole is variable from one sill to another but
312 are nearly homogeneous within the same sill. K-feldspar phenocrysts are common and
313 often occur elongate or with lobate boundaries (Fig. 9d). Quartz grains generally show
314 undulose extinction and occur as recrystallized, 0.1 - 0.5 mm-sized grains with sutured
315 boundaries (Fig. 9c). Allanite and titanite occur as accessory phases in granodiorites and
316 monzogranites, as inclusions in K-feldspar phenocrysts or in contact with biotite and calcic
317 amphiboles. Euhedral coarse garnet, titanite and biotite and disseminated pyrite,
318 molybdenite and chalcopyrite are common in syenogranites and pegmatite bodies.
319 Prismatic elongated zircons to small, rounded zircons are present. Biotite chloritization is
320 common and mainly observed in the samples with a brownish-red colour in the field. This
321 alteration is more frequently found near fault zones, especially in the central and northern
322 quarries of the marble district (CL, FD and AT areas; Fig. 1b). Chloritites formed after
323 intense hydrothermal alteration at c. 300°C of A2 felsic apophyses is found in the
324 northernmost quarry (CL area) (Reis et al., 2017; Hoerlle et al., 2023).

325 **5.3. Skarns**

326 **5.3.1. Diopside skarns**

327 The diopside skarns consist of white to green aggregates of diopside (\pm calcite \pm
328 tremolite \pm Fe-Cu-Mo sulphides) typically forming irregularly shaped boudin and pinch-
329 and-swell structures (Figs. 4a-c) within the marbles or locally bordering only A1 mafic
330 apophyses (Figs. 3c-d). When bordering the A1 mafic apophyses they show variable
331 thicknesses on each border of the apophysis (Figs. 3c-d) and are often present at one
332 border of the sill only. The coarse grained diopsides are commonly replaced by medium to
333 fine grained tremolite and serpentine. Diopside skarns were not observed bordering A2
334 felsic apophyses. The diopside skarns occur mostly parallel to the metamorphic foliation
335 (S_1), are rarely folded with the marble layers, and often replace marble mylonitic layers
336 (Fig. 4a). The thickness of diopside skarns varies from a few centimetres reaching more

337 than 50 cm, with the majority ranging from 3 to 15 cm. They are commonly bordered by
338 forsterite skarns (Figs. 3a; 4b-c). The coarse diopside grains or aggregates that vary from
339 millimetre to centimetre sized crystals. They host pyrite, pyrrhotite, molybdenite,
340 micrometre sized calcite and tremolite and rarely phlogopite inclusions. Where fracturing is
341 more intense, diopside grains tend to be divided into sub-grains and partially replaced by
342 millimetre sized tremolite and calcite, which also crystallize along the grain boundaries and
343 fractures. Modal abundances of diopside, tremolite, and calcite in diopside skarns vary
344 significantly from 70-100% diopside, 0-17% tremolite and 0-13% calcite. Diopside grain
345 boundaries are sharp when in contact with coarse grained forsterite-zone (Figs. 10a-b) or
346 irregular/corroded when bordered by fine grained trails of forsterite (Figs. 10a,c). Locally,
347 diopside grains are partially to fully replaced by antigorite.

348 **5.3.2. Forsterite skarns**

349 The forsterite skarns comprise the most common and widespread skarn type that
350 often border diopside skarns (Figs. 3a,c,d and 4b-c), A1 and A2 apophyses (Fig. 3b) or
351 occur as isolated lenses (Figs. 3b-c and 4a). Even though they are mostly oriented parallel
352 to the metamorphic foliation, forsterite skarns often crosscut the foliation A1 or occur as
353 thicker aggregates near felsic apophyses terminations (Fig. 3b). This skarn type comprises
354 a forsterite + calcite zone (forsterite zone) bordered by phlogopite + dolomite + calcite
355 zone (phlogopite zone).

356 The forsterite zone consists of μm to mm rounded forsterite clusters in a calcite
357 matrix forming planar arrays. Coarser grained forsterite clusters are mostly located in low-
358 strain zones whereas thin arrays with micrometric forsterite trails are in higher strain zones
359 (Fig. 4c). Rounded olivine grains occur in an irregularly shaped calcite matrix (Fig. 10a). In
360 general, the modal distribution between forsterite and calcite is 65% to 35%, respectively.
361 Anhedral pyrite often occurs disseminated in the calcite matrix of the forsterite zone. The
362 calcite matrix shows variable amounts of dolomite exsolution. Commonly, small lamellae of

363 phlogopite occurs within the forsterite zone. Rarely, the forsterite zone contains green
364 spinel and chlorite aggregates. Most locations have portions of partially preserved to fully
365 replaced forsterite. Macroscopic black rounded grains are preserved olivine whereas
366 green to light green rounded grains are partially or fully replaced by serpentine.
367 Serpentinization is more intense near brittle structures and mainly fault zones. The degree
368 of serpentinization is generally homogeneous within the same sample but variable in
369 different samples.

370 At the outer portion of the forsterite skarns, the phlogopite zone is composed of
371 fine-grained light-brown to colourless phlogopite in a white dolomite + calcite matrix. This
372 zone is always present between the forsterite zone and the dolomitic marble. Its thickness
373 varies roughly proportionally to the width of the respective forsterite zone. The transition
374 from the forsterite zone to the phlogopite zone is irregular and the main changes are the
375 variation from a calcite to a mainly dolomitic matrix, the absence of forsterite and the
376 increase in the abundance and grain size of phlogopite (Fig. 10a). The carbonates in the
377 phlogopite zone form a granoblastic texture with elongate subhedral to euhedral dolomites
378 whereas irregular-shaped calcite occurs along dolomite or phlogopite grain boundaries
379 (Fig. 10d). The dolomite and phlogopite are generally oriented parallel with the same
380 orientation of the forsterite arrays and boundaries of the diopside skarns. The modal
381 abundances of phlogopite vary from 5 to 15%, 5-10% of calcite and 80-90% of dolomite.
382 The phlogopite zone differs from the host dolomitic marbles mainly in silicate content
383 (tremolite and talc in host rocks versus phlogopite in skarns) and microstructures (sutured
384 dolomite grains in host rocks versus elongate polygonal dolomite in the phlogopite zone).
385 Phlogopite is a typical mica occurring in magnesian skarns worldwide (Meinert et al., 2005;
386 Sieber et al., 2020). Phlogopite is partially to fully replaced by antigorite in retrograded
387 samples.

388 **5.4. Hydrothermal veins and breccias**

389 Distinct fracture filling veins, stockworks and breccias are present within the area.
390 They are mostly found in the north of the marble quarry district (CL area; Fig. 1b) where
391 they occur a few to tens of meters away from subvertical NW trending fault zones and
392 areas of brittle deformation, mainly crosscutting the metamorphic foliation and skarns (Fig.
393 5a). They are not folded and commonly form stockworks (Figs. 5b-c). They consist of
394 centimetre sized veins with coarse euhedral calcite crystals and massive chalcopyrite and
395 pyrite aggregates cemented by chlorite and calcite (Figs. 5b-c). Locally, veins can reach
396 more than 30 cm of thickness and coarser calcite crystals exceed 5 cm. Symmetrical rims
397 around the veins are characterized by high abundance of serpentine within a few
398 centimetres into the host marble (Figs. 5a-d). Breccias are composed of marble fragments
399 and coarse subhedral calcites cemented by massive chlorite, pyrite, and chalcopyrite (Fig.
400 5d).

401 **6. LA-ICP-MS U-Pb GEOCHRONOLOGY**

402 **6.1. Zircon U-Pb ages**

403 **6.1.1. A1 mafic apophyses**

404 Zircons from a foliated fine grained mafic apophysis (DB area; DB-G1Z sample;
405 location shown in Fig. 3b) have an average length of c. 120 μm and a maximum of 170
406 μm . The aspect ratio varies from 2:1 to 3:1 and the zircon crystals are dominantly sub-
407 rounded (Fig. 11d). Grains are either unzoned or irregularly sector zoned. Twenty
408 discordant grains combined with five concordant zircons formed a discordia line that
409 yielded an upper intercept $^{207}\text{Pb}/^{206}\text{Pb}$ age of 1787 ± 14 Ma (MSWD = 2.4; Fig. 11b; Table
410 S1). Three discordant analyses combined with three concordant grains formed another
411 discordia line that resulted in an upper intercept $^{207}\text{Pb}/^{206}\text{Pb}$ age of 2190 ± 20 Ma (MSWD =
412 0.64; Fig. 11b; Table S1). Both Paleoproterozoic ages are interpreted as inherited ages.
413 Previous geochronology studies in the Caçapava do Sul Granitic Complex indicated

414 inherited zircon grains with ages ranging from 2.7 Ga to 0.7 Ga (Leite et al., 1998; Remus
415 et al., 2000).

416 **6.1.2. A2 felsic apophysis**

417 A total of 28 zircons were separated and analysed from a gray medium grained
418 biotite-hornblende granodiorite (DB area; DB-G2Z sample; location shown Fig. 3b). The
419 grains are mostly prismatic and have an average length of c. 215 μm and aspect ratio of
420 4:1 reaching up to a maximum of 340 μm and 6:1, respectively (igneous zircons of Fig.
421 11c). Twenty-two analyses on prismatic zircon grains with concentric or patchy CL zoning
422 including cores and rims (Fig. 11c) yielded a concordia $^{206}\text{Pb}/^{238}\text{U}$ age of 578.0 ± 4.7 Ma
423 (MSWD = 4.5; N = 22; Fig. 11a; Table S2) interpreted as the magmatic age of the sill. Two
424 spots on prismatic grains with concentric zoning are highly discordant (10 and 62% conc.);
425 and four smaller subrounded grains (Fig. 11c) yield inherited concordant ages of 611 ± 18 ;
426 1231 ± 16 , 1733 ± 45 and 2045 ± 25 Ma.

427 **6.2. Apatite and titanite ages**

428 **6.2.1. Mafic apophysis (A1)**

429 Titanites were separated from a mafic apophysis sample (AT area; AT-Z-01
430 sample) in a quarry-scale fold hinge area. The rock is composed of actinolite (27%), biotite
431 (23%), K-feldspar (24%) plagioclase (21%) and quartz (3%) with titanite, apatite, pyrite as
432 common accessory phases and very fine-grained zircon as traces. Titanite occurs included
433 in biotite and amphiboles or along their grain boundaries (Figs. 7c; 8a-b). Size of analysed
434 grains ranges from 100 to 200 μm . Biotite and apatite are commonly included in the
435 titanite, which also host allanite, rutile, and quartz inclusions (Fig. 8d). BSE imaging shows
436 simple or patchy zoning in the titanites. Twenty grains were analysed aiming to cover
437 different zones. A Tera-Wasserburg plot of titanite analytical results define a discordant
438 array with a lower intercept on the concordia at 556.1 ± 2.9 Ma ($\text{Pbc S/K} = 0.869$; MSWD =
439 1.2; N = 20; Fig. 12a; Table S3).

440 Apatite samples were separated from two A1 mafic apophyses (AT area; AT-Z-02;
441 AT-Z-03) that are mainly composed of phlogopite (40%), actinolite (40%), plagioclase
442 (20%) and apatite as main accessory phase. The analysed apatite grains are mainly
443 prismatic, colourless, and have an average size of c. 150 μm reaching up to a maximum of
444 270 μm . They occur mainly in the grain boundaries with the same preferred orientation of
445 the actinolite and phlogopite, but also included in the amphibole and plagioclase (Figs. 8e-
446 f). BSE and CL imaging revealed the absence of zoning and inclusions in the apatite
447 crystals. The Tera-Wasserburg plots of apatite analytical results define discordant arrays
448 with lower intercepts on the concordia at 557.8 ± 3.4 Ma (Pbc S/K = 0.873; MSWD = 0.97;
449 N = 20; Fig. 12b; Table S4) and 557.0 ± 4.9 Ma (Pbc S/K = 0.873; MSWD = 0.51; N = 18;
450 Fig. 12c; Table S5).

451 7. DISCUSSION

452 7.1. Igneous emplacement sequence, geochronology, and related tectonics

453 Crosscutting relationships and structural patterns of the igneous apophyses suggest
454 that A1 mafic and felsic apophyses intruded the marbles and were subsequently deformed
455 (Figs. 2a-d; 14a-b). A different set of unfolded thicker felsic sills (> 2 m; A2) emplaced in
456 the axial planes of A1 apophyses indicate that larger volumes of felsic magmatism
457 intruded the marbles in a second event after the A1 intrusions (Fig. 14b). The orientation of
458 the A2 apophyses and the preferred orientation of the minerals within these intrusions are
459 parallel to the S_2 metamorphic foliation and the axial surfaces of the A1 folded intrusions.
460 Many A2 apophyses show features that indicate folding during the intrusion (e.g., Fig. 6b)
461 hence A2 was synkinematic to the S_2 forming event, which was previously proposed by
462 Nardi & Bitencourt (1989) who describe an igneous foliation throughout the granitic
463 batholith parallel to the S_2 foliation of the PFMC and suggests that most of the batholith
464 was syntectonic. A1 mafic apophyses were not described in the inner portions of the
465 granitic batholith which suggests that most of the body was assembled by the A2 felsic

466 apophyses and subsequent intrusions and that A1-related magmatism had restricted
467 volume. Field aspects and mineral assemblages of A1 mafic apophyses suggest that
468 these rocks were metamorphosed after a mafic protolith. However, their composition and
469 structural response are distinct from typical metabasalts. High amounts of biotite and
470 amphibole (up to 80%) and the co-existence of hydrous Mg-rich minerals with K-feldspar
471 and quartz are uncommon in metabasalts. A recent study shows that A1 mafic apophyses
472 were initially mafic rocks (i.e., basalts) that were metamorphosed and altered during the
473 intrusion of A2 felsic intrusions of the Caçapava do Sul Granitic Complex (Hoerlle et al.,
474 2022).

475 Attempts to obtain a magmatic age for the A1 mafic apophyses resulted in inherited
476 ages only (sample DB-G1Z; Figs. 3c and 11b). The composite character of the mafic-felsic
477 intrusive bodies indicates a contemporaneous intrusion of the A1 felsic and mafic
478 apophyses (Figs. 6a). A similar bimodal character with contemporaneous mafic and felsic
479 volcanism between 600 and 580 Ma has been described in the region associated with an
480 extensional regime during the early stages of the development of the Camaquã Basin
481 (Wildner et al., 1999; Janikian et al., 2012; Oliveira et al., 2014). Therefore, we interpret
482 the A1 mafic-felsic intrusions as correlated to this extensional magmatism. Bimodal
483 magmatism typically occurs in extensional environments in various tectonic settings (e.g.,
484 Hochstaedter et al., 1990; Jolly et al., 2008). We interpret the A1 intrusions in an overall
485 extensional setting between 600 and 580 Ma hence mafic apophyses are likely limited to
486 this time span. The age of 578 ± 4.7 Ma was obtained for a A2 felsic apophysis, which is
487 interpreted to be formed during a compressive regime. Therefore, the transition from an
488 extensional related mafic-felsic magmatism (A1) to a compressional regime with felsic-
489 dominated magmatism (A2) occurred most likely between 590 and 580 Ma.

490 The complexity of deciphering the magmatic source of the Caçapava do Sul
491 Granitic Complex was highlighted in previous studies (Nardi & Bitencourt 1989; Babinski et

492 al., 1996; Remus et al., 2000; Hoerlle et al., 2022). To the same end, the variable inherited
493 zircon populations identified in the A2 felsic apophysis, A1 mafic apophysis and in
494 previous studies (Leite et al. 1998; Remus et al., 2000) equally point towards a
495 heterogeneous magmatic source. Inherited zircon grains of c. 600 Ma were identified in
496 the A2 felsic apophysis and in granodiorites from previous studies (Remus et al., 2000),
497 which suggests that igneous rocks from the preceding magmatic event were also sources
498 for the A2 magma.

499 The consistent ages obtained from titanite and apatite from three A1 mafic
500 apophyses samples suggest that the U-Pb closure or resetting of these minerals occurred
501 at c. 557 Ma. Titanite and apatite have different Pb closure temperatures typically of 500-
502 650°C (e.g., Cherniak, 1993) and 375-600°C (e.g., Cochrane et al., 2014) respectively.
503 Since both minerals record the same age within the error, it is likely that the isotopic
504 closure occurred below 500°C. Additionally, apatite is considered highly susceptible to
505 metasomatic processes at variable pressures and temperatures (e.g., Spear & Pyle, 2002;
506 Harlov, 2015; Kirkland et al., 2018). Field relationships show that the A1 mafic apophyses
507 crystallized before the S₂ forming event and the intrusion of A2 felsic apophyses (A2 is
508 synkinematic to S₂). Therefore, the age recorded by titanite and apatite cannot represent
509 the age of the crystallization of the A1 mafic apophyses. If we consider that A1 magmatism
510 occurred at some point between 600 and 580 Ma and A2 at c. 578 Ma, another source of
511 heat and fluids is needed at c. 557 Ma to reset the titanite and apatite. Two possible
512 explanations are presented for the age recorded in titanite and apatite. We interpret that
513 previously dated intrusions of c. 560 Ma (Leite et al., 1998; Remus et al., 2000) represent
514 a different magmatic pulse and heat from this episode resets the titanite and apatite in the
515 A1 mafic apophyses. In this case, protracted magmatism was responsible for the
516 assembly of the granitic complex with a finite number of discrete pulses with cooling
517 between pulses. Protracted assembly of plutons is recognized worldwide and commonly

518 results in overprinted granites with heterogeneous textures and chemistry (e.g., He et al.,
519 2018; Tichomirowa et al., 2019). The last pulse that heated the wallrocks and caused fluid
520 infiltration led to resetting of the titanite and apatite dates in the A1 mafic apophyses at c.
521 557 Ma.

522 Alternatively, the A2 apophysis and previously dated intrusions of Leite et al. (1998)
523 and Remus et al. (2000) represent ages of the incremental intrusion of felsic magmas from
524 c. 578 to 562 Ma resulting in the assembly of the CSGC. The heat from continuous
525 intrusions maintains elevated temperatures ($>500^{\circ}$) in the system, results in
526 metamorphism of the A1 mafic apophyses and opens the isotopic system for titanite and
527 apatite. The age of 557 Ma is recorded in apatite and titanite when magmatism ceased
528 and temperature dropped below c. 500°C , defining the late magmatic stage of the system.
529 However, if this alternative hypothesis is correct, temperatures within the batholith and
530 inner aureole were maintained continuously at $>500^{\circ}\text{C}$ for c. 20 My. This implies that the
531 thermal aureole surrounding the batholith would be very wide. The discussion of the width
532 of the thermal aureole is out of the scope of this paper and future studies of the aureole
533 may provide useful insights into the hypothesis of a continuously assembled batholith over
534 20 My. Nevertheless, both alternatives suggest that the CSGC was assembled from
535 several intrusions from c. 578 to 557 Ma and that apatite and titanite record the age of late
536 magmatism in the area (Fig. 14a-c).

537 **7.2. Multistage fluid influx and associated metasomatic rocks reveals**
538 **details of intrusion history of the syntectonic Caçapava do Sul Granitic**
539 **Complex**

540 Magnesian skarns commonly have similar assemblages of those formed during
541 isochemical metamorphism of impure dolomites. Here, evidence indicate that the skarn
542 assemblages were formed from the infiltration of magmatic fluids in opposition to
543 isochemical metamorphism for the following reasons: (i) spatial coincidence of skarn

bodies and igneous apophyses (Figs. 2d and 3a-d); (ii) the skarns locally crosscut the S_0 bedding and the S_1 regional metamorphic foliation (Figs. 2g and 3a); (iii) minor occurrence and finer-grained silicate phases (tremolite and talc) in the unreacted dolomite parts versus coarse-grained diopside and forsterite in the skarns; and (iv) presence of molybdenite, pyrite and pyrrhotite associated with the skarns (Figs. 10a-b). The presence of the sulphides in the skarns (Fig. 10a) indicates the presence of Fe, Mo, Cu and other metals dissolved in the magmatic fluid in addition to silica. We note, however, that previous studies in magnesian skarns indicate that the main skarn minerals such as forsterite, diopside, or periclase do not contain significant amounts of iron; hence, the iron in solution tends to form oxides or sulphides rather than andradite or hedenbergite, for example (Hall et al., 1988).

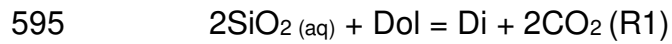
The two main groups of metasomatic rocks (skarns and hydrothermal veins and breccias) hosted by the marbles of the Passo Feio Metamorphic Complex are associated with two main stages of the crystallization history of the Caçapava do Sul Granitic Complex. The di- and fo-skarns are considered to be formed during the emplacement of A2 felsic intrusions because (i) they are seen both along A2 and A1 contacts (Figs. 3a-d and 14b; A2 is younger than A1, see section 7.1); (ii) they show deformation features following S_2 formation (e.g., sigmoidal extension veins; Fig. 2g) and (iii) they are common at S_2 fold hinges (Fig. 3d and 14b; A2 is syntectonic to the S_2 forming event). In addition, field relationships indicate that formation of the forsterite skarns is related to the emplacement of the pegmatitic portions of the A2 felsic apophyses, and the spatial patterns of pegmatites and forsterite skarns highlight the source and pathways of the fluids (Fig. 3b and b'). Hence, we consider that the age of the forsterite skarns can be directly associated with the age of the adjacent A2 felsic apophysis of 578 ± 4.7 Ma (sample DB-G2Z; Fig. 3b).

569 The second group of metasomatic rocks, the calcite-chlorite-sulphide veins and
570 breccias (Fig. 5a-d), is associated with cooling and uplift of the granitic complex at the end
571 of the magmatic activity because of the lower temperature of the vein assemblages
572 (chlorite, antigorite) and the abundant Fe-Cu sulphide content, previously associated with
573 the late hydrothermal activity of the CSGC (Remus et al., 2000; Reis et al., 2017). The age
574 of the lower-T hydrothermal veins and breccias formation is associated with the cooling
575 event recorded in titanite and apatite at c. 557 Ma. The genesis and evolution of each
576 stage is discussed in the sections below.

577 **7.2.1. Diopside and forsterite skarn formation associated with A2 felsic** 578 **intrusions**

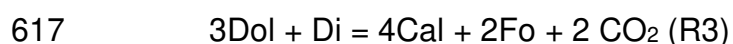
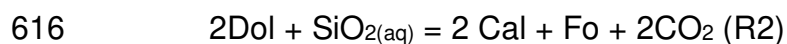
579 The diopside and forsterite skarns occur as either isolated bodies (e.g., Figs. 3b
580 and 4a) or, more commonly, zoned di-fo-skarns (e.g., Figs. 3a; 3c-d; 4b-c). We note that
581 when isolated, the size of the skarn is much smaller compared to the zoned di-fo-skarns.
582 Isolated forsterite skarns occur typically as mm- to cm-sized arrays and are more common
583 than isolated diopside skarns. Given that diopside and forsterite are (i) frequently
584 combined; (ii) occur along similar interfaces, both spatially close to A2 apophyses; (iii)
585 show similar deformation patterns and (iv) both are stable at high temperatures (e.g., 600
586 °C), we consider that they most likely formed during the same event. Considering that, we
587 interpret that the variations in fluid composition (e.g., aSiO₂; XCO₂) or fluid flux are the
588 controlling factors governing the formation of different assemblages.

589 In the diopside skarns, tremolite is only found as a minor phase along diopside
590 fractures and texturally interpreted to be a product of retrogression. The retrogressive
591 tremolite is different from the tremolite grains found in the unaltered impure dolomitic
592 marbles formed during the prior regional metamorphism (e.g., Goulart et al., 2013). Hence,
593 we interpret the prograde formation of diopside to proceed via a reaction of dolomite with
594 SiO₂-bearing fluids released from the cooling apophyses:



596 This reaction will be a function of pressure, temperature, $X(\text{CO}_2)$ and $a(\text{SiO}_2)$ conditions.
597 Previous studies suggest pressures between 0.45 and 0.5 GPa for the A2 emplacement
598 conditions, based on the presence of igneous muscovite in the felsic apophyses by Nardi
599 & Bitencourt (1989) and amphibole-plagioclase geobarometry calculations (Hoerlle et al.,
600 2023). There are no direct constraints yet available on temperature of formation of the
601 diopside skarn. However, studies of calcite inclusions in forsterite from forsterite skarns in
602 the same area reported temperatures between 590 and 630 °C for the crystallization of
603 forsterite and calcite (Hoerlle et al., 2019; 2023). In addition, previous fluid inclusion
604 studies indicate that, in general, the temperature of skarn formation varies from 100 °C to
605 650 °C (Bodnar et al., 2013). Assuming that di-skarns did not form at lower temperature
606 than fo-skarns, we argue that the diopside formed at a minimum temperature of 590°C. At
607 this condition, the diopside could form either at high values for $X(\text{CO}_2) > 0.8$ (Fig. 13a;
608 arrow 1) or at low values for $X(\text{CO}_2) < 0.2$ and low values for $a(\text{SiO}_2)$ from ~0.2 to ~0.5
609 (Fig. 13a; arrow 3).

610 Forsterite and calcite likely resulted from the reaction of aqueous silica and dolomite
611 (R2) forming isolated fo-skarns or after diopside + dolomite (R3) bordering the diopside
612 skarns. The formation of metasomatic reaction veins during fluid infiltration is a well-
613 established concept (e.g., Bucher-Nurminen, 1981; Bégué et al., 2019). In addition, the
614 metastable formation of forsterite directly from dolomite and silica was previously reported
615 by Müller et al. (2004) and Ferry et al. (2011).



618 The outer phlogopite zone that borders fo-skarns comprises recrystallized dolomite and
619 phlogopite with interstitial calcite (Fig. 10d). The transition from the forsterite zone to the
620 phlogopite zone can be explained by the propagating reaction front lowering silica activity

621 that leads to the partial dissolution and reprecipitation of the dolomite + calcite. The
622 remaining amount of Si and other elements dissolved in the fluid (e.g., K, Fe, F) were
623 incorporated in the phlogopite crystallizing along grain boundaries of the carbonates.

624 There is textural evidence documenting the sequential development of diopside,
625 followed by forsterite + calcite and dolomite + phlogopite + calcite. In the zoned skarns, the
626 formation of forsterite was a consequence of changes in either fluid composition or fluid
627 flux. The skarn formation itself is inherently linked to physicochemical conditions and the
628 amount and composition of the infiltrating fluid and thus, the spatial and field observations
629 can be used to decipher the infiltration history recorded in the transition from diopside
630 skarns to forsterite skarns. However, at least two main alternative interpretations can be
631 used to explain the observed sequence.

632 The observed sequence could be explained by changes of the effective fluid flux
633 (Fig. 15; Scenario 1), i.e., the amount of fluid flux over time during the infiltration event
634 governing the effective water-to-rock ratio (W/R). While the effect of scale- and path-
635 dependent W/R ratios have been successfully used to explain spatial variations in the
636 amount of oxygen isotope shifts observed in hydrothermal systems (Bowman et al., 1987),
637 a similar concept could be envisaged for temporal changes within a propagating reaction
638 front. Here, a very limited amount of fluid resulting in a high molar fraction of CO₂ in the
639 fluid ($X(\text{CO}_2)$) leads to formation of diopside by the breakdown of dolomite and aqueous
640 silica (Fig. 13a; arrow 1). The system is initially internally buffered at high $X(\text{CO}_2)$ values
641 (>0.8) requiring high Si-activities between 0.9 and 1 to form diopside (Fig. 13a; arrow 1).
642 At these conditions, slightly lower $X(\text{CO}_2)$ values would result in the formation of prograde
643 tremolite (Fig. 13a), which is not observed in the skarns. Subsequently, forsterite
644 crystallization could be facilitated by continued fluid infiltration or subsequent pulses
645 increasing the effective fluid flux, lowering the $X(\text{CO}_2)$ and shifting the system into an
646 externally buffered regime at low $X(\text{CO}_2)$ conditions (Fig. 13a; arrow 2). The formation of

647 forsterite from diopside and dolomite can occur at approximately the same temperature
648 ($\sim 600^{\circ}\text{C}$), but at lower $X(\text{CO}_2) < 0.06$ and $a(\text{SiO}_2) < 0.15$ (Fig. 13a; arrow 2). Such a ‘dry’
649 heating stage with subsequent infiltration causing a shift in mineral reactions has
650 previously been reported in contact aureoles involving impure dolomites (Müller et al.,
651 2004).

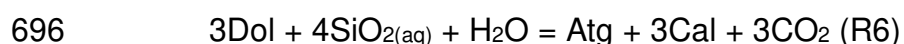
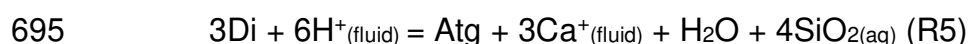
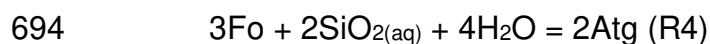
652 In a second scenario (Fig. 15; Scenario 2), the observed sequence of diopside –
653 forsterite – dolomite could be explained by constant fluid flux at low $X(\text{CO}_2)$ conditions and
654 variable $a\text{SiO}_2$ (Fig. 15; S2). In this context, diopside would be formed first at low $X(\text{CO}_2)$
655 ($0.06 < X\text{CO}_2 < 0.17$) and low silica activity ($0.15 < a\text{SiO}_2 < 0.35$; Fig. 13a; arrow 3). The
656 subsequent formation of forsterite can be explained by limited Si-mobility along the
657 propagating reaction front (Fig. 13a – arrow 2; Fig. 13b – arrow 4) as suggested by Bégué
658 et al. (2020). We note that it is also possible that this reaction could result from cooling
659 (e.g., Fig. 13b – arrow 5; Fig. 13c – arrow 6). However, it is unlikely that a significant
660 temperature drop would occur within a few centimetres during the formation of the zoned
661 di-fo-skarns. On the other hand, the Si-concentration of the igneous fluid is indeed likely to
662 be limited depending on its solubility and composition of the igneous rock it has
663 equilibrated with before infiltration into the country rocks. We note that the dolomitic
664 marbles contain minor silicate phases. Their conversion to skarn would require either
665 substantial SiO_2 concentrations (very large volume reduction of the dolomite
666 accompanying skarn formation) or large time-integrated fluid fluxes (TIFF – see
667 Baumgartner & Rumble, 1988) if SiO_2 is introduced by an infiltrating igneous fluid.

668 In concluding this section, we note that the succession of zoned skarn formation
669 starting with diopside followed by forsterite + calcite can be explained in two ways
670 regarding the effective fluid flux but both result in variations in $a\text{SiO}_2$ and $X\text{CO}_2$ conditions.
671 Additionally, we highlight that the observed heterogeneity of the “isolated” diopside or
672 forsterite only versus “zoned” diopside-forsterite-skarns can also be explained by the

673 process of variable fluid flux and composition. While additional geochemical data such as
674 isotope signatures, mass balance constraints, estimates of time integrated fluid fluxes are
675 needed to quantitatively answer some of the open questions regarding the infiltration
676 history, such an analysis would be beyond the scope of this conceptual paper and will thus
677 be addressed in follow-up contributions.

678 **7.2.2. Hydrothermal veins and breccias and skarn retrometamorphism:**
679 **cooling of the granitic complex and late fluid circulation leads to**
680 **serpentinization and chloritization**

681 After the final magmatic intrusions crystallized at c. 557 Ma and temperature
682 dropped, the host rocks, skarns and A1 and A2 apophyses started to deform in a brittle
683 manner (Fig. 14c). Late-cooling granites and pegmatites are interpreted as the source for
684 H₂O-rich fluids that infiltrated brittle structures and previous pathways (Fig. 6d and 14c).
685 Hydrothermal chloritization of biotite in granodiorites of the granitic complex occurred at c.
686 300°C (Reis et al., 2017; Hoerlle et al., 2023). We interpret that the serpentinization of
687 skarns (Fig. 5e) occurred at similar conditions because the calcite-chlorite-veins are
688 bordered by antigorite and calcite in the host rock and temperature ranges for
689 serpentinization and chloritization are similar. Silica and water-rich fluids use faults,
690 fractures and marble-skarn interfaces as pathways leading to the serpentinization of
691 forsterite and diopside (Fig. 5e and 14c) according to reactions 4 and 5. Fully
692 serpentinized skarns are symmetrically bordered by massive green antigorite marbles up
693 to a few meters (e.g., Fig. 5e).



697 In both reactions, the volume change of the solids is positive. Additionally, at 300°C
698 the serpentinization rate is highest (Martin & Fyfe, 1970). Fracturing occurs because the
699 higher the reaction rate, the faster the volume of affected rock increases and there is little
700 time to accommodate the stress resulting from volume increase (Jamtveit & Hammer,
701 2012). Serpentinization of the skarn assemblages is more intense near faults (<100 m)
702 which indicates high fluid flux through the brittle structures. Serpentinization resulted in
703 positive feedback between reaction-driven cracking and fluid infiltration that replaces all
704 the prograde silicate assemblages of the skarn (Fig. 5e). Remaining fluids infiltrate into the
705 adjacent cracked dolomites leading to the formation of antigorite and calcite from dolomite
706 and aqueous siliceous fluids (R6). Therefore, the second metasomatic stage corresponds
707 to a retrogressive stage and differs from the prior stages associated with the main
708 magmatic phase of skarn formation.

709 **7.3. Heterogeneity and asymmetry in metasomatic rocks: evidence of** 710 **localized and heterogeneous fluid flow**

711 The skarn-forming flow paths comprise mainly contrasting lithological contacts such
712 as apophysis-marble interfaces (Figs. 3b-d), S₂ foliation planes within the carbonates
713 (Figs. 3b) and fold hinges (Fig. 3d). Thus, the arrays of isolated diopside and forsterite
714 skarns as well as the zoned diopside + forsterite skarns (Fig. 14a) are interpreted to be
715 formed due to fluid flow at preexisting weak surfaces in addition to structurally controlled
716 areas in the marbles or contacts (Fig. 14b). The asymmetry of skarns bordering
717 apophyses (e.g., Fig. 3c) and the lack preferred occurrence of skarns in the upper or lower
718 borders of the apophyses indicate that the fluid flow was localized and very
719 heterogeneous. Therefore, the fact that locations of skarn formation are very
720 heterogeneously distributed and that the size of skarns are highly varied require an a-priori
721 highly heterogeneous fluid flow scenario where fluid availability is limited and
722 heterogeneous in space, volume, and composition. These observations therefore are

723 consistent with a one fluid flux event, with general limited fluid flux which results in local
724 variability in fluid volume and associated composition as well as fluid ingress location.

725 Lithological and structurally controlled fluid flow during metamorphism and
726 deformation is a well-acknowledged phenomenon (e.g., Skelton et al., 1995; Pitcairn et al.,
727 2010). A similar forsterite-calcite assemblage formed parallel to carbonate foliation has
728 been previously reported as the result of fluid flow and metasomatism along foliation-
729 parallel deformation enhanced permeability by Holness (1997). Formation of pinch-and-
730 swell structures, boudinage and folding enhanced the porosity at these interfaces and
731 created positive feedback of deformation and fluid influx during the S₂ forming event.
732 Brittle failure as a necessary part of both boudinage and pinch-and-swell structures was
733 demonstrated by Gardner et al. (2015). The occurrence of diopside and forsterite skarns in
734 sigmoidal extension veins (Fig. 2g) and along the fold hinge zones (Figs. 3a and d)
735 suggests a S₂ synkinematic origin. Additionally, microstructures show that the forsterite
736 and phlogopite zones are oriented parallel to the diopside skarn pinch-and-swell
737 boundaries (Fig. 10a). Yet, recrystallization of dolomite “adjusting” its orientation parallel to
738 the fluid pathways in the phlogopite zone suggests that the recrystallization was fluid-
739 mediated as reported similarly by Holness (1997). We note that due to strength contrast
740 between pyroxene and olivine diopside can behave as brittle and forsterite as ductile
741 during the same deformation event. Coarse-grained forsterite and calcite are found in
742 strain shadows (Fig. 10a and b) suggesting that they likely formed synchronous to the
743 deformation event that resulted in boudinage and pinch-and-swell structures. Field
744 observations and microstructures also suggest that as the diopside skarn bands broke
745 brittle and that fluid infiltration led to forsterite and calcite crystallization within the fractured
746 diopside grains (Figs. 4b-c and 10a). Hence the relative timing with earlier diopside
747 followed by forsterite + calcite yet formed during a single event (Fig. 14b).

748 In the second metasomatic stage (hydrothermal veins and breccias), subvertical
749 faults and fractures cross-cutting previous structures created new pathways for fluid flow
750 (Fig. 14c). Fault zones are structures for fluid flow and act as localized conduits (e.g.,
751 Dipple & Ferry, 1992; Caine et al., 1996). The calcite-chlorite-sulphide veins and breccias
752 in the granitic complex wallrocks (Figs. 5a,c and e) indicate fluid flow associated with the
753 brittle structures (Fig. 14c). However, the serpentinization of skarn assemblages suggest
754 that the fluids also used pre-existing pathways (Fig. 5e).

755 In summary, fluid flow patterns throughout the metasomatic stages foresee: (i) fluid
756 flow along foliation planes, lithological boundaries and through axial zones in the first stage
757 (Figs. 2d; 3a-c and 14b) and (ii) hydrofracturing and retrogression associated to fluid flow
758 through fractures and fault zones in the second stage (Figs. 5a-c and 14c).

759 **7.4. Using localized metasomatic reactions to decipher intrusion history:** 760 **challenges and opportunities**

761 Magmatic systems where fluid source, deformation, geometry, and timing
762 constraints of the pluton are complex can be challenging to decipher and thus restrain the
763 description of the sequence of events (e.g., Caçapava do Sul Granitic Complex). The
764 different metasomatic rocks formed after the interaction of the Caçapava do Sul Granitic
765 Complex and the marbles of the Passo Feio Metamorphic Complex helped to reveal
766 different stages of the history of the granitic complex. Contrasting emplacement models
767 were proposed, including a diapir-like (Nardi & Bitencourt, 1989), a sheet-like intrusion
768 (Fragoso-César, 1991), a lens-shaped syntectonic batholith (Fernandes et al., 1992) and
769 an intrusion along a fault-bend-fold of a right lateral strike-slip shear zone (Costa et al.,
770 1995). However, the study of the metasomatic rocks formed at different stages supported
771 by field relationships, petrography and geochronological data suggests that the granitic
772 complex was likely assembled by several pulses during a c. 21 My time interval, at least.
773 Additionally, skarns formed during different deformational regimes suggest that the first

774 intrusions (A1) were formed under an extensional regime before c. 578 Ma followed by
775 folding and affected by the heat and fluids of subsequent felsic magmatism from 578 Ma
776 until c. 557 Ma, marking the reduction of tectonic activity and the end of magmatism (Fig.
777 14b-c). Our findings agree with the proposals that large igneous bodies can be formed by
778 the protracted or incremental supply of magma build up over millions of years (e.g.,
779 Petford et al., 2000; Coleman et al., 2004; He et al., 2018; Tichomirowa et al., 2019).

780 Field and petrographical recognition of incrementally assembled plutons is difficult
781 because conditions can prevail near the original magmatic temperatures for a long time,
782 potentially obscuring pristine contacts between individual increments (Bartley et al., 2008).
783 In this contribution, we have shown that studying the metasomatic reactions can be useful
784 to unveil different stages of the intrusion history of a complex magmatic body. This is
785 particularly elucidative when carbonate rocks are present near the intrusion resulting in the
786 formation of skarns. These rocks form distinct microstructures and mineral assemblages
787 that can be related to the different stages of a pluton crystallization (Meinert et al., 2005).
788 However, this is challenging because working with multistage fluid-rock interaction
789 requires dealing with complicated overlapping of processes that can partially or totally
790 erase previous features.

791 In addition to the field relations and microstructures, dating minerals formed or reset
792 during metamorphism and fluid infiltration (e.g., apatite and titanite) is a valuable tool in
793 deciphering the timing constraints of fluid circulation during magmatic emplacement, even
794 if they generally record the latest magmatic or fluid infiltration event in those rocks. Yet,
795 precise dating of all metasomatic stages is impracticable, especially in magnesian skarn
796 systems where the lack of datable phases is common. In calcic skarn systems, however,
797 the direct dating of a metasomatic phase is achievable mainly when grossular-andradite
798 garnet is present (e.g., Deng et al., 2017; Gevedon et al., 2018). Identifying precise
799 intervals and duration of metasomatic processes in magnesian skarn systems remains

800 challenging whereas integrated studies of magmatic zircon of the causative intrusion and
801 metasomatic phases in metamorphic rocks provide a timespan for the pluton assembly.
802 Finally, studying the metasomatic reactions commonly observed in the host rocks and
803 apophyses of a magmatic complex provides useful insights on deformation and timing of
804 pluton assembly and associated fluid activity.

805 **ACKNOWLEDGEMENTS**

806 This work was supported by CNPq-National Council for Scientific and Technological
807 Development of Brazil (Proc. 141333/2017-0) and CAPES-PRINT (Proc.
808 88887.467220/2019-00). We thank Dagoberto Barcelos, Inducal, Ativa Minerais, Mônego,
809 FIDA, Razzera, Vigor and Cruzeiro companies for access to the marble quarries. Gilberto
810 Santos and Lidia Vignol are thanked for zircon, titanite and apatite sample preparation and
811 Gabriel Monaco for field assistance. We thank John R. Bowman for constructive criticism
812 on a previous version of the manuscript.

813 **REFERENCES**

- 814 Aleinikoff, J.N., Wintsch, R.P., Tollo, R.P., Unruh, D.M., Fanning, C.M., Schmitz, M.D.,
815 2007. Ages and origins of rocks of the Killingworth dome, south-central Connecticut:
816 Implications for the tectonic evolution of southern New England. *American Journal*
817 *of Science* 307, 63–118. <https://doi.org/10.2475/01.2007.04>
- 818 Babinski, M., Chemale, F., Hartmann, L.A., Van Schmus, W.R., Carlos da Silva, L.,
819 1996. Juvenile accretion at 750–700 Ma in southern Brazil. *Geology* 24, 439.
820 [https://doi.org/10.1130/0091-7613\(1996\)024<0439:JAAMIS>2.3.CO;2](https://doi.org/10.1130/0091-7613(1996)024<0439:JAAMIS>2.3.CO;2)
- 821 Bartley, J.M., Coleman, D.S., Glazner, A.F., 2008. Incremental pluton emplacement by
822 magmatic crack-seal. *Transactions of the Royal Society of Edinburgh: Earth*
823 *Sciences* 97, 383–396. <https://doi.org/10.1017/S0263593300001528>

824 Baumgartner, L.P., Rumble, D., 1988. Transport of stable isotopes: I: Development of a
 825 kinetic continuum theory for stable isotope transport. *Contributions to Mineralogy
 826 and Petrology* 98, 417–430. <https://doi.org/10.1007/BF00372362>
 827 Bégué, F., Baumgartner, L.P., Bouvier, A.-S., Robyr, M., 2019. Reactive fluid infiltration
 828 along fractures: Textural observations coupled to in-situ isotopic analyses. *Earth
 829 and Planetary Science Letters* 519, 264–273.
 830 <https://doi.org/10.1016/j.epsl.2019.05.024>
 831 Bégué, F., Baumgartner, L.P., Müller, T., Putlitz, B., Vennemann, T.W., 2020.
 832 Metasomatic Vein Formation by Stationary Fluids in Carbonate Xenoliths at the
 833 Eastern Margin of the Bergell Intrusion, Val Sissone, Italy. *Journal of Petrology* 60,
 834 2387–2412. <https://doi.org/10.1093/petrology/egaa012>
 835 Bicalho, V., Remus, M.V.D., Rizzardo, R., Dani, N., 2019. Geochemistry, metamorphic
 836 evolution and tectonic significance of metabasites from Caçapava do Sul, southern
 837 Brazil. *Brazilian Journal of Geology* 49, 1–16. [https://doi.org/10.1590/2317-
 838 4889201920180039](https://doi.org/10.1590/2317-4889201920180039)
 839 Bitencourt, M.F., 1983. *Geologia petrologia e estrutura dos metamorfitos da região de*
 840 *Caçapava do Sul, RS. Universidade Federal do Rio Grande do Sul.*
 841 Bodnar, R.J., Lecumberri-Sanchez, P., Moncada, D., Steele-MacInnis, M., 2014. Fluid
 842 Inclusions in Hydrothermal Ore Deposits, in: *Treatise on Geochemistry*. Elsevier,
 843 pp. 119–142. <https://doi.org/10.1016/B978-0-08-095975-7.01105-0>
 844 Bortolotto, O.J., 1988. Metamorfismo termal dos mármore de Caçapava do Sul, RS.
 845 *Ciência e Natura* 10, 25. <https://doi.org/10.5902/2179460X25479>
 846 Bowman, J.R., Parry, W.T., Kropp, W.P., Kruer, S.A., 1987. Chemical and isotopic
 847 evolution of hydrothermal solutions at Bingham, Utah. *Economic Geology* 82, 395–
 848 428. <https://doi.org/10.2113/gsecongeo.82.2.395>

849 Brown, P.E., Bowman, J.R., Kelly, W.C., 1985. Petrologic and stable isotope
 850 constraints on the source and evolution of skarn-forming fluids at Pine Creek,
 851 California. *Economic Geology* 80, 72–95.
 852 <https://doi.org/10.2113/gsecongeo.80.1.72>

853 Bucher-Nurminen, K., 1981. The formation of metasomatic reaction veins in dolomitic
 854 marble roof pendants in the Bergell Intrusion (Province Sondrio, northern Italy).
 855 *American Journal of Science* 281, 1197–1222.
 856 <https://doi.org/10.2475/ajs.281.9.1197>

857 Buddington, A.F., 1959. Granite Emplacement With Special Reference to North
 858 America. *GSA Bulletin* 70, 671–747. [https://doi.org/10.1130/0016-](https://doi.org/10.1130/0016-7606(1959)70[671:GEWSRT]2.0.CO;2)
 859 [7606\(1959\)70\[671:GEWSRT\]2.0.CO;2](https://doi.org/10.1130/0016-7606(1959)70[671:GEWSRT]2.0.CO;2)

860 Caine, J.S., Evans, J.P., Forster, C.B., 1996. Fault zone architecture and permeability
 861 structure. *Geology* 24, 1025. [https://doi.org/10.1130/0091-](https://doi.org/10.1130/0091-7613(1996)024<1025:FZAAPS>2.3.CO;2)
 862 [7613\(1996\)024<1025:FZAAPS>2.3.CO;2](https://doi.org/10.1130/0091-7613(1996)024<1025:FZAAPS>2.3.CO;2)

863 Cerva-Alves, T., Remus, M.V.D., Dani, N., Basei, M.A.S., 2017. Integrated field,
 864 mineralogical and geochemical characteristics of Caçapava do Sul alvikite and
 865 beforite intrusions: A new Ediacaran carbonatite complex in southernmost Brazil.
 866 *Ore Geology Reviews* 88, 352–369.
 867 <https://doi.org/10.1016/j.oregeorev.2017.05.017>

868 Cherniak, D.J., 1993. Lead diffusion in titanite and preliminary results on the effects of
 869 radiation damage on Pb transport. *Chemical Geology* 110, 177–194.
 870 [https://doi.org/10.1016/0009-2541\(93\)90253-F](https://doi.org/10.1016/0009-2541(93)90253-F)

871 Clemens, J.D., Mawer, C.K., 1992. Granitic magma transport by fracture propagation.
 872 *Tectonophysics* 204, 339–360. [https://doi.org/10.1016/0040-1951\(92\)90316-X](https://doi.org/10.1016/0040-1951(92)90316-X)

873 Cochran, R., Spikings, R.A., Chew, D., Wotzlaw, J.-F., Chiaradia, M., Tyrrell, S.,
874 Schaltegger, U., Van der Lelij, R., 2014. High temperature (>350°C)
875 thermochronology and mechanisms of Pb loss in apatite. *Geochimica et*
876 *Cosmochimica Acta* 127, 39–56. <https://doi.org/10.1016/j.gca.2013.11.028>

877 Coleman, D.S., Gray, W., Glazner, A.F., 2004. Rethinking the emplacement and
878 evolution of zoned plutons: Geochronologic evidence for incremental assembly of
879 the Tuolumne Intrusive Suite, California. *Geology* 32, 433.
880 <https://doi.org/10.1130/G20220.1>

881 Connolly, J.A.D., 1990. Multivariable phase diagrams; an algorithm based on
882 generalized thermodynamics. *American Journal of Science* 290, 666–718.
883 <https://doi.org/10.2475/ajs.290.6.666>

884 Cordani, U.G., Halpern, N., Berenholc, M., 1974. Idades Radiométricas de Rochas do
885 Escudo Sul-Riograndense e sua Significação Tectônica. X Carta do Brasil ao
886 Milionésimo, Folha de Porto Alegre. Porto Alegre

887 Costa, A.F.U., Fernandes, L.A.D., Shukowsky, W., Nardi, L.V.S., Bitencourt, M.F.,
888 2018. Teste dos Modelos Tectônicos e de Posicionamento do Complexo Granítico
889 de Caçapava do Sul Através de Estudos de Modelagem Gravimétrica 3-D. *Revista*
890 *Brasileira de Geofísica* 13. <https://doi.org/10.22564/rbgf.v13i2.1185>

891 Deng, X.-D., Li, J.-W., Luo, T., Wang, H.-Q., 2017. Dating magmatic and hydrothermal
892 processes using andradite-rich garnet U–Pb geochronometry. *Contributions to*
893 *Mineralogy and Petrology* 172, 71. <https://doi.org/10.1007/s00410-017-1389-2>

894 Dipple, G.M., Ferry, J.M., 1992. Metasomatism and fluid flow in ductile fault zones.
895 *Contributions to Mineralogy and Petrology* 112, 149–164.
896 <https://doi.org/10.1007/BF00310451>

897 Engvik, A.K., Taubald, H., Solli, A., Grenne, T., Austrheim, H., 2018. Dynamic
 898 Metasomatism: Stable Isotopes, Fluid Evolution, and Deformation of Albitite and
 899 Scapolite Metagabbro (Bamble Lithotectonic Domain, South Norway). *Geofluids*
 900 2018, 1–22. <https://doi.org/10.1155/2018/9325809>

901 Fernandes, L.A.D., Tommasi, A., Porcher, C.C., 1992. Deformation patterns in the
 902 southern Brazilian branch of the Dom Feliciano Belt: A reappraisal. *Journal of South*
 903 *American Earth Sciences* 5, 77–96. [https://doi.org/10.1016/0895-9811\(92\)90061-3](https://doi.org/10.1016/0895-9811(92)90061-3)

904 Ferry, J.M., Ushikubo, T., Valley, J.W., 2011. Formation of Forsterite by Silicification of
 905 Dolomite during Contact Metamorphism. *Journal of Petrology* 52, 1619–1640.
 906 <https://doi.org/10.1093/petrology/egr021>

907 Fragoso-César, A.R.S., 1991. Tectônica de placas no ciclo brasileiro: as orogenias
 908 dos cinturões Dom Feliciano e Ribeira no Rio Grande do Sul. Universidade de São
 909 Paulo, São Paulo. <https://doi.org/10.11606/T.44.1991.tde-23042013-162133>

910 Gardner, R.L., Piazzolo, S., Daczko, N.R., 2015. Pinch and swell structures: evidence
 911 for strain localisation by brittle–viscous behaviour in the middle crust. *Solid Earth* 6,
 912 1045–1061. <https://doi.org/10.5194/se-6-1045-2015>

913 Gevedon, M., Seman, S., Barnes, J.D., Lackey, J.S., Stockli, D.F., 2018. Unraveling
 914 histories of hydrothermal systems via U–Pb laser ablation dating of skarn garnet.
 915 *Earth and Planetary Science Letters* 498, 237–246.
 916 <https://doi.org/10.1016/j.epsl.2018.06.036>

917 Goulart, R.V., Remus, M.V.D., Reis, R.S., 2013. Composição isotópica de Sr, C e O e
 918 geoquímica de ETRs das rochas carbonáticas do Bloco São Gabriel, Rio Grande
 919 do Sul. *Pesquisas em Geociências* 40, 75–97.

920 Hall, D.L., Cohen, L.H., Schiffman, P., 1988. Hydrothermal alteration associated with
 921 the Iron Hat iron skarn deposit, eastern Mojave Desert, San Bernardino County,
 922 California: *Economic Geology* 83, 568–587.

923 Harlov, D.E., 2015. Apatite: A Fingerprint for Metasomatic Processes. *Elements* 11,
 924 171–176. <https://doi.org/10.2113/gselements.11.3.171>

925 Hartmann, L.A., Leite, J.A.D., Da Silva, L.C., Remus, M.V.D., McNaughton, N.J.,
 926 Groves, D.I., Fletcher, I.R., Santos, J.O.S., Vasconcellos, M.A.Z., 2000. Advances
 927 in SHRIMP geochronology and their impact on understanding the tectonic and
 928 metallogenic evolution of southern Brazil. *Australian Journal of Earth Sciences* 47,
 929 829–844. <https://doi.org/10.1046/j.1440-0952.2000.00815.x>

930 Hartmann, L.A., Philipp, R.P., Santos, J.O.S., McNaughton, N.J., 2011. Time frame of
 931 753–680Ma juvenile accretion during the São Gabriel orogeny, southern Brazilian
 932 Shield. *Gondwana Research* 19, 84–99. <https://doi.org/10.1016/j.gr.2010.05.001>

933 Hartmann, L.A., Tindle, A., Bitencourt, M.F., 1990. O metamorfismo de fácies anfibolito
 934 no Complexo Metamórfico Passo Feio, RS, com base em química dos minerais.
 935 *Pesquisas* 17, 62–71. <https://doi.org/10.22456/1807-9806.21383>

936 He, C., Gong, S., Wang, L., Chen, N., Santosh, M., Wang, Q., 2018. Protracted post-
 937 collisional magmatism during plate subduction shutdown in early Paleoproterozoic:
 938 Insights from post-collisional granitoid suite in NW China. *Gondwana Research* 55,
 939 92–111. <https://doi.org/10.1016/j.gr.2017.11.009>

940 Hochstaedter, A.G., Gill, J.B., Kusakabe, M., Newman, S., Pringle, M., Taylor, B.,
 941 Fryer, P., 1990. Volcanism in the Sumisu Rift, I. Major element, volatile, and stable
 942 isotope geochemistry. *Earth and Planetary Science Letters* 100, 179–194.
 943 [https://doi.org/10.1016/0012-821X\(90\)90184-Y](https://doi.org/10.1016/0012-821X(90)90184-Y)

944 Hoerlle, G.S., Remus, M.V.D., Gomes, M.E.B., 2019. Geothermometry of the
 945 Caçapava do Sul magnesian skarns: insights from calcite inclusions in forsterite.
 946 Presented at the IV Simpósio Brasileiro de Metalogenia. Gramado, Brazil.

947 Hoerlle, G.S., Vinicius, M., Remus, D., Dani, N., 2022. Metamafic dyke and sill swarms
 948 in the Dom Feliciano Belt : Insights for post-collisional strike-slip tectonics and fluid-
 949 assisted metamorphism. *Precambrian Research* 383, 106906.
 950 <https://doi.org/10.1016/j.precamres.2022.106906>

951 Hoerlle, G.S., Remus, M.V.D., Dani, N., Silva, M.A.L., Lana, C., 2023. Post-collisional
 952 magmatic-hydrothermal mineralization in the São Gabriel Terrane (southern Brazil):
 953 Insights from mineral chemistry, stable isotopes, and sulfide trace-elements of the
 954 Caçapava do Sul skarns. *Journal of South American Earth Sciences* 123. 104203.
 955 <https://doi.org/10.1016/j.jsames.2023.104203>

956 Holland, T.J.B., Powell, R., 2011. An improved and extended internally consistent
 957 thermodynamic dataset for phases of petrological interest, involving a new equation
 958 of state for solids. *Journal of Metamorphic Geology* 29, 333–383.
 959 <https://doi.org/10.1111/j.1525-1314.2010.00923.x>

960 Holness, M.B., 1997. Fluid flow paths and mechanisms of fluid infiltration in carbonates
 961 during contact metamorphism: the Beinn an Dubhaich aureole, Skye. *Journal of*
 962 *Metamorphic Geology* 15, 59–70. <https://doi.org/10.1111/j.1525-1314.1997.00005.x>

963 Jackson, S.E., Pearson, N.J., Griffin, W.L., Belousova, E.A., 2004. The application of
 964 laser ablation-inductively coupled plasma-mass spectrometry to in situ U–Pb zircon
 965 geochronology. *Chemical Geology* 211, 47–69.
 966 <https://doi.org/10.1016/j.chemgeo.2004.06.017>

967 Jamtveit, B., Hammer, Ø., 2012. Sculpting of Rocks by Reactive Fluids. *Geochemical*
 968 *Perspectives* 1, 341–481. <https://doi.org/10.7185/geochempersp.1.3>

969 Janikian, L., Almeida, R.P., Fragoso-César, A.R.S., Martins, V.T. de S., Dantas, E.L.,
 970 Tohver, E., McReath, I., D'Agrella-Filho, M.S., 2012. Ages (U–Pb SHRIMP and LA
 971 ICPMS) and stratigraphic evolution of the Neoproterozoic volcano-sedimentary
 972 successions from the extensional Camaquã Basin, Southern Brazil. *Gondwana*
 973 *Research* 21, 466–482. <https://doi.org/10.1016/j.gr.2011.04.010>
 974 Jolly, W.T., Lidiak, E.G., Dickin, A.P., 2008. Bimodal volcanism in northeast Puerto
 975 Rico and the Virgin Islands (Greater Antilles Island Arc): Genetic links with
 976 Cretaceous subduction of the mid-Atlantic ridge Caribbean spur. *Lithos* 103, 393–
 977 414. <https://doi.org/10.1016/j.lithos.2007.10.008>
 978 Kinny, P.D., McNaughton, N.J., Fanning, C.M., Maas, R., 1994. 518 Ma Sphene
 979 (Titanite) from the Khan Pegmatite, Namibia, Southwest Africa: a potential ion-
 980 microprobe standard. Presented at the 8th International Conference on
 981 Geochronology, Cosmochronology and Isotope Geology, 1107, p.171.
 982 Kirkland, C.L., Yakymchuk, C., Szilas, K., Evans, N., Hollis, J., McDonald, B., Gardiner,
 983 N.J., 2018. Apatite: a U-Pb thermochronometer or geochronometer? *Lithos* 318–
 984 319, 143–157. <https://doi.org/10.1016/j.lithos.2018.08.007>
 985 Leite, J.A.D., Hartman, L.A., Mcnaughton, N.J., Chemale, F., 1998. SHRIMP U/Pb
 986 Zircon Geochronology of Neoproterozoic Juvenile and Crustal-Reworked Terranes
 987 in Southernmost Brazil. *International Geology Review* 40, 688–705.
 988 <https://doi.org/10.1080/00206819809465232>
 989 Lopes, C.G., Pimentel, M.M., Philipp, R.P., Gruber, L., Armstrong, R., Junges, S.,
 990 2015. Provenance of the Passo Feio complex, Dom Feliciano Belt: Implications for
 991 the age of supracrustal rocks of the São Gabriel Arc, southern Brazil. *Journal of*
 992 *South American Earth Sciences* 58, 9–17.
 993 <https://doi.org/10.1016/j.jsames.2014.11.004>

- Ludwig, K. R., 2003. User's manual for Isoplot 3.00, a geochronological toolkit for Microsoft Excel. Berkeley Geochronology Center special publication no.4. Components.
- Martin, B., Fyfe, W.S., 1970. Some experimental and theoretical observations on the kinetics of hydration reactions with particular reference to serpentinization. Chemical Geology 6, 185–202. [https://doi.org/10.1016/0009-2541\(70\)90018-5](https://doi.org/10.1016/0009-2541(70)90018-5)
- Meinert, L.D., Dipple, G.M., Nicolescu, S., 2005. World Skarn Deposits, in: One Hundredth Anniversary Volume. Society of Economic Geologists. <https://doi.org/10.5382/AV100.11>
- Miller, R.B., Paterson, S.R., 1999. In defense of magmatic diapirs. Journal of Structural Geology 21, 1161–1173. [https://doi.org/10.1016/S0191-8141\(99\)00033-4](https://doi.org/10.1016/S0191-8141(99)00033-4)
- Müller, T., Baumgartner, L.P., Foster, C.T., Vennemann, T.W., 2004. Metastable prograde mineral reactions in contact aureoles. Geology 32, 821. <https://doi.org/10.1130/G20576.1>
- Nabelek, P.I., Bédard, J.H., Hryciuk, M., Hayes, B., 2013. Short-duration contact metamorphism of calcareous sedimentary rocks by Neoproterozoic Franklin gabbro sills and dykes on Victoria Island, Canada. Journal of Metamorphic Geology 31, 205–220. <https://doi.org/10.1111/jmg.12015>
- Nardi, L.V.S., Bitencourt, M. de F., 1989. Geologia, Petrologia e Geoquímica do Complexo Granítico de Caçapava do Sul, RS. Revista Brasileira de Geociências 19, 153–169. <https://doi.org/10.25249/0375-7536.1989153169>
- Oliveira, C.H.E., Chemale, F., Jelinek, A.R., Bicca, M.M., Philipp, R.P., 2014. U–Pb and Lu–Hf isotopes applied to the evolution of the late to post-orogenic transtensional basins of the dom feliciano belt, Brazil. Precambrian Research 246, 240–255. <https://doi.org/10.1016/j.precamres.2014.03.008>

- Petford, N., Cruden, A.R., McCaffrey, K.J.W., Vigneresse, J.-L., 2000. Granite magma formation, transport and emplacement in the Earth's crust. *Nature* 408, 669–673. <https://doi.org/10.1038/35047000>
- Pitcairn, I.K., Skelton, A.D.L., Broman, C., Arghe, F., Boyce, A., 2010. Structurally focused fluid flow during orogenesis: the Islay Anticline, SW Highlands, Scotland. *Journal of the Geological Society* 167, 659–674. <https://doi.org/10.1144/0016-76492009-135>
- Reis, R.S., Remus, M.V.D., Dani, N., Anzolin, H.D.M., 2018. Alteração clorítica no flanco leste do Granito Caçapava, Rio Grande do Sul: evolução do metassomatismo e sulfetos de Cu-Fe associados. *Geologia USP. Série Científica* 17, 61. <https://doi.org/10.11606/issn.2316-9095.v17-121013>
- Remus, M.V.D, Hartmann, L.A., McNaughton, N., Groves, D., Fletcher, I., 2000. The link between hydrothermal epigenetic copper mineralization and the Caçapava Granite of the Brasiliano Cycle in southern Brazil. *Journal of South American Earth Sciences* 13, 191–216. [https://doi.org/10.1016/S0895-9811\(00\)00017-1](https://doi.org/10.1016/S0895-9811(00)00017-1)
- Remus, M.V.D., Hartmann, L.A., Formoso, M.L.L., 1993. Os padrões de elementos terras raras (ETR) e a afinidade geoquímica komatiítica dos xistos magnesianos e rochas associadas do Complexo Cambaizinho, São Gabriel/RS. *Revista Brasileira de Geociências* 23, 370–387. <https://doi.org/10.25249/0375-7536.1993234370387>
- Remus, M.V.D., Massonne, H., Hartmann, L.A., Theye, T., Braetz, H., 2010. Garnet zonation and monazite ages as monitors of contrasting metamorphic evolution in the Brasiliano schist belts of Southern Brazil. 45 Congresso Brasileiro de Geologia.
- Saalmann, K., Gerdes, A., Lahaye, Y., Hartmann, L.A., Remus, M.V.D., Läufer, A., 2011. Multiple accretion at the eastern margin of the Rio de la Plata craton: the

1043 prolonged Brasiliano orogeny in southernmost Brazil. *International Journal of Earth*
1044 *Sciences* 100, 355–378. <https://doi.org/10.1007/s00531-010-0564-8>

1045 Santos, M.M., Lana, C., Scholz, R., Buick, I., Schmitz, M.D., Kamo, S.L., Gerdes, A.,
1046 Corfu, F., Tapster, S., Lancaster, P., Storey, C.D., Basei, M.A.S., Tohver, E.,
1047 Alkmim, A., Nalini, H., Krambrock, K., Fantini, C., Wiedenbeck, M., 2017. A New
1048 Appraisal of Sri Lankan BB Zircon as a Reference Material for LA-ICP-MS U-Pb
1049 Geochronology and Lu-Hf Isotope Tracing. *Geostandards and Geoanalytical*
1050 *Research* 41, 335–358. <https://doi.org/10.1111/ggr.12167>

1051 Sartori, P.L.P., Kawashita, K., 1985. Petrologia e geocronologia do Batólito Granítico
1052 de Caçapava do Sul-RS. In *II Simpósio Sul-Brasileiro de Geologia* (pp. 102–115).
1053 Florianópolis, Brazil

1054 Sieber, M.J., Brink, F.J., Leys, C., King, P.L., Henley, R.W., 2020. Prograde and
1055 retrograde metasomatic reactions in mineralised magnesium-silicate skarn in the
1056 Cu-Au Ertzberg East Skarn System, Ertzberg, Papua Province, Indonesia. *Ore*
1057 *Geology Reviews* 125, 103697. <https://doi.org/10.1016/j.oregeorev.2020.103697>

1058 Silva-Filho, B.C., Matsdorf, M., 1987. Análise estrutural dos metamorfitos da borda
1059 oeste do Granito Caçapava, Caçapava do Sul: implicações geológicas locais e
1060 regionais. In *Atas do III Simpósio Sul-Brasileiro de Geologia*. Curitiba, Brazil.

1061 Skelton, A.D.L., Graham, C.M., Bickle, M.J., 1995. Lithological and Structural Controls
1062 on Regional 3-D Fluid Flow Patterns during Greenschist Facies Metamorphism of
1063 the Dalradian of the SW Scottish Highlands. *Journal of Petrology* 36, 563–586.
1064 <https://doi.org/10.1093/petrology/36.2.563>

1065 Sláma, J., Košler, J., Condon, D.J., Crowley, J.L., Gerdes, A., Hanchar, J.M.,
1066 Horstwood, M.S.A., Morris, G.A., Nasdala, L., Norberg, N., Schaltegger, U.,
1067 Schoene, B., Tubrett, M.N., Whitehouse, M.J., 2008. Plešovice zircon — A new

1068 natural reference material for U–Pb and Hf isotopic microanalysis. *Chemical*
1069 *Geology* 249, 1–35. <https://doi.org/10.1016/j.chemgeo.2007.11.005>

1070 Spear, F.S., Pyle, J.M., 2002. Apatite, Monazite, and Xenotime in Metamorphic Rocks.
1071 *Reviews in Mineralogy and Geochemistry* 48, 293–335.
1072 <https://doi.org/10.2138/rmg.2002.48.7>

1073 Spear, F.S., Pyle, J.M., 2002. Apatite, Monazite, and Xenotime in Metamorphic Rocks.
1074 *Reviews in Mineralogy and Geochemistry* 48, 293–335.
1075 <https://doi.org/10.2138/rmg.2002.48.7>

1076 Thompson, J., Meffre, S., Maas, R., Kamenetsky, V., Kamenetsky, M., Goemann, K.,
1077 Ehrig, K., Danyushevsky, L., 2016. Matrix effects in Pb/U measurements during LA-
1078 ICP-MS analysis of the mineral apatite. *Journal of Analytical Atomic Spectrometry*
1079 31, 1206–1215. <https://doi.org/10.1039/C6JA00048G>

1080 Thomson, S.N., Gehrels, G.E., Ruiz, J., Buchwaldt, R., 2012. Routine low-damage
1081 apatite U-Pb dating using laser ablation-multicollector-ICPMS. *Geochemistry,*
1082 *Geophysics, Geosystems* 13, n/a-n/a. <https://doi.org/10.1029/2011GC003928>

1083 Tichomirowa, M., Käßner, A., Sperner, B., Lapp, M., Leonhardt, D., Linnemann, U.,
1084 Münker, C., Ovtcharova, M., Pfänder, J.A., Schaltegger, U., Sergeev, S., von
1085 Quadt, A., Whitehouse, M., 2019. Dating multiply overprinted granites: The effect of
1086 protracted magmatism and fluid flow on dating systems (zircon U-Pb:
1087 SHRIMP/SIMS, LA-ICP-MS, CA-ID-TIMS; and Rb–Sr, Ar–Ar) – Granites from the
1088 Western Erzgebirge (Bohemian Massif, Germany). *Chemical Geology* 519, 11–38.
1089 <https://doi.org/10.1016/j.chemgeo.2019.04.024>

1090 Van Achterbergh, E., Ryan, C.G., Jackson, S.E. Griffin, W.L., 2001. Data reduction
1091 software for LA-ICP-MS, in: Paul, J.S. (Ed.), *Laser-Ablation-ICPMS in the Earth*

1092 Sciences: Principles and Applications, Mineralogical Association of Canada,
1093 Ottawa, pp. 239–243.

1094 Whitney, D.L., Evans, B.W. 2010. Abbreviations for names of rock-forming minerals.
1095 American Mineralogist 95(1), 185–187. <https://doi.org/10.2138/am.2010.3371>

1096 Wildner, W., Nardi, L.V.S., Lima, E.F., 1999. Post-Collisional Alkaline Magmatism on
1097 the Taquarembó Plateau: A Well-Preserved Neoproterozoic–Cambrian Plutono-
1098 volcanic Association in Southern Brazil. International Geology Review 41, 1082–
1099 1098. <https://doi.org/10.1080/00206819909465193>

1100

SUPPORTING INFORMATION

Additional Supporting Information may be found online in the supporting information tab for this article.

Description:

Table S1. Results of LA-ICP-MS zircon U–Pb analysis for A1 mafic apophysis (DB-G1Z sample)

Table S2. Results of LA-ICP-MS zircon U–Pb analysis for A2 felsic apophysis (DB-G2Z sample)

Table S3. Results of LA-ICP-MS titanite U–Pb analysis for A1 mafic apophysis (AT-Z-01 sample)

Table S4. Results of LA-ICP-MS apatite U–Pb analysis for A1 mafic apophysis (AT-Z-02 sample)

Table S5. Results of LA-ICP-MS apatite U–Pb analysis for A1 mafic apophysis (AT-Z-03 sample)

Figure S6: Additional calculated Schreinemarkers diagrams showing the effects of variations of T, P and $a\text{SiO}_2$ on relevant diopside and forsterite forming reactions and stability fields

FIGURE CAPTIONS

Fig. 1: Location of the CSGC and PPMC in the Sul-riograndense shield, southern Brazil. (a) Tectonic domains of the Sul-riograndense Shield (TT: Tijucas Terrane; SGT: São Gabriel Terrane; PB: Pelotas Batholith; CB: Camaquã Basin; TQ: Taquarembó Terrane). (b and c) Geological map and cross-section of the PPMC and CSGC area showing main structural data and sampling locations.

Fig. 2: General field relations and structures of the dolomitic marbles of the PPMC and igneous apophyses of the CSGC. (a) General view of the marble quarry in the AT area showing folded marble (white dashed lines) forming major recumbent folds and concordant to subconcordant intrusions of A1 felsic and mafic apophyses; truck (approximate height 5 m) for scale. (b) Folded parallel intrusions of A1 apophyses with sub-horizontal N-S axis in the DB area; person (1.8 m) for scale. (c) Outcrop photo (top) and detailed sketch (bottom) of folded A1 mafic apophyses parallel to the subhorizontal N-S trending axial plane in the CL area. (d) Outcrop photo (top) and detailed sketch (bottom) of the A1 mafic and felsic apophyses parallel to the marble foliation and synkinematic di-fo-skarn formation at the termination of the mafic apophysis in the CL area; notepad (25 cm) for scale. (e) tight recumbent isoclinal fold in the dolomitic marble and intrusion of A1 mafic and felsic apophyses parallel to the axial plane in the AT area; (f) intercalation of high-strain “mylonites” and low-strain layers highlighting the S_1 foliation in the marbles; coin (diameter 3 cm) for scale. (g) tension gashes filled with di-fo-skarns in a brittle-ductile shear zone parallel to the axial planes (S_2) of marble folding in the CL area; compass for scale.

Fig. 3: Outcrop scale relations of A1 and A2 apophyses and associated skarns. (a) Outcrop photo (left) and detailed sketch (right) of diopside skarns in pinch-and-swell structures bordered by forsterite skarns formed perpendicular to irregular terminations of A2 felsic apophyses in the DB area. Location of the representative microstructures of the

1145 zoned skarns in Fig. 10a marked by red rectangle. (b) Outcrop photo (left) and detailed
1146 sketch (right) of forsterite skarns formed in lithological contacts and foliation-parallel
1147 fractures within the marbles from fluids released from the pegmatitic portion of a A2 felsic
1148 apophysis. Yellow arrows indicate fluid pathways and possible flow direction. Stars in the
1149 left side image indicate the location of geochronological samples. Hammer (~40 cm) for
1150 scale. (c) Asymmetric skarn formation bordering mafic apophysis in the AT area. White
1151 lines indicate apophysis-skarn boundaries; red lines indicate the boundary between
1152 diopside and forsterite skarns. Apophysis thickness of approximately 20 cm. (d) Folded
1153 mafic apophysis and associated zoned skarn formation at CL area; hammer (~35 cm) for
1154 scale.

1155 Fig. 4: Field aspects of skarns. (a) Lenticular di- and fo skarns parallel to S_1 foliation
1156 of the marbles; diopside pinch-and-swell in high strain area; Brown colors indicate
1157 “crushed” unconsolidated fine-grained carbonates; hammer (40 cm) for scale. (b) Zoned
1158 asymmetric di-fo-skarns with broken diopside boudin/pinch-and-swell structure bordered
1159 by forsterite and phlogopite zones; blue pen lid (4 cm) for scale. (c) Outcrop photograph
1160 (left) in DB area and detailed sketch (right) showing contrasting shapes and grain sizes in
1161 zoned skarns caused by strain contrast; broken diopside in pinch-and-swell structure
1162 bordered by coarser forsterite (lower strain areas) versus thin elongate diopside band
1163 bordered by fine grained forsterites in DB area. Note fo-cal within diopside fragments and
1164 dashed lines indicating local fractures in the pinch-and-swell structure.

1165 Fig. 5: Macroscopic features of calcite-chlorite-sulphide veins and fully
1166 serpentized skarns. (a) Outcrop photograph (left) and detailed sketch (right) showing
1167 calcite-chlorite-sulphide veins bordered by antigorite and calcite perpendicular to marble
1168 S_1 foliation; veins hosted within green antigorite-marbles with primary antigorite in a
1169 calcite-dolomite matrix located near NW-SE subvertical fault zone in the CL area. (b-c)
1170 Calcite-chlorite stockworks bordered by antigorite + calcite reaction fronts; 6 cm pen lid for

1171 scale. (d) Cal-chl-sulphide breccia with marble and coarse calcite fragments cemented by
1172 chlorite and sulphides; CL area; coin for scale. (e) fully serpentinized di-fo-skarns and
1173 antigorite-marbles.

1174 Fig. 6: Macroscopic features of A1 and A2 apophyses. (a) Composite A1 mafic-
1175 felsic apophysis with pinch-and-swell felsic enclaves in A1 mafic apophysis (AT area);
1176 hammer (~45 cm) for scale; (b) A2 felsic apophyses with mafic enclave and synmagmatic
1177 folding; (c) Detail of the A2 felsic rock with elongate K-feldspar grains and thin biotite
1178 layers defining the foliation indicated by white dashed lines; (d) Thick and late felsic
1179 intrusion (late A2) crosscutting A1 and A2 tabular apophyses.

1180 Fig. 7: Microstructures of A1 mafic apophyses: (a) Photomicrograph of a bt-pl-hbl
1181 schist showing spaced foliation with intercalation of plagioclase and hornblende
1182 aggregates separated by discontinuous lenticular aggregates of biotite; chloritized biotite in
1183 a micro shear zone in the right side of the image; scale bar: 5 mm; PPL. AT area (b) Wide
1184 photomicrograph of pl-act-bt schist showing sigmoidal biotite intercalated with aggregates
1185 of plagioclase and actinolite marking S₂ foliation of the mafic apophysis, subtle crenulation
1186 (black dashed lines); scale bar: 5 mm; PPL; CL area. (c) Photomicrograph of a pl-bt-kfs-
1187 amp schist showing preferred orientation of biotite and elongated actinolite marking the S₂
1188 foliation; short prisms of hornblende; subhedral titanites in the grain boundaries of biotite
1189 with K-feldspar or amphiboles; AT area; scale bar: 0.5 mm; XPL. (d) Photomicrograph of a
1190 pl-bt-act schist showing spaced foliation marked by intercalation of anastomosing biotite
1191 and elongate actinolite aggregates with small (<0.2 mm) grains of plagioclase in between
1192 the amphiboles. AT area; scale bar: 0.5 mm; XPL.

1193 Fig. 8: Backscattered electron (BSE) images of representative microstructures and
1194 highlighted accessory phases of A1 mafic apophyses; in yellow: titanite; in red: apatite. (a)
1195 Microstructures of pl-bt-kfs-hbl-act showing subhedral titanite included in biotite
1196 aggregates, small rounded grains of titanite included in hornblende and rounded and

1197 anhedral titanite in the grain boundaries of biotite with K-feldspar, plagioclase or
1198 amphibole; sample AT-Z-01; AT area; scale bar: 0.25 mm. (b-c) Microstructures of pl-bt-
1199 act schists showing apatite included in actinolite, next to plagioclases and included in
1200 plagioclase; samples AT-Z-02 and AT-Z-03, respectively; AT area; scale bar: 0.25 mm. (d)
1201 Internal structures and inclusions of titanite grains; sample AT-Z-01; AT area; scale bar:
1202 100 μ m.

1203 Fig. 9: Microstructures of A1 and A2 felsic apophyses. (a) Photomicrograph of a A1
1204 felsic apophysis showing a fine-grained quartzo-felspathic matrix and abundant biotite.
1205 Scale bar: 0.5 mm. XPL. (b) BSE image of A1 felsic apophysis showing preferential
1206 orientation of biotite in a Kfs-qz-pl matrix. Scale bar: 0.2 mm. (c) Photomicrograph of a hbl-
1207 bt-granodiorite (A2) showing mirmekites (green arrow); quartz with sutured grain
1208 boundaries (red arrows) and undulose extinction (blue arrows); cross-polarized light (XPL);
1209 scale bar: 0.5 mm; sample DB-G2Z from DB area shown in Fig. 3b. (d) Photomicrograph
1210 of a bt-monzogranite (A2) showing K-feldspar porphyrocrysts with lobate boundaries,
1211 quartz with undulose extinction (blue arrows) and sutured boundaries (red arrows) from AT
1212 area. Scale bar: 0.5 mm. XPL.

1213 Fig. 10: Microstructures of a zoned di-fo-skarn, similar to the microstructures
1214 illustrated in Fig. 3a at a smaller scale. (a) general view of the skarn zones in a thin section
1215 scale, dashed white lines indicate location of Figs. 10b-d; scale bar: 5 mm, XPL; (b) di and
1216 coarse euhedral fo (~4 mm) in equilibrium with a cal matrix in a strain shadow zone;
1217 rounded tr inclusions in di; subhedral py in the cal matrix; scale bar: 0.5 mm. (c) fo- zone
1218 with fine-grained rounded fo arrays (<0.2 mm) in cal matrix and coarser fo (~0.5 mm)
1219 partially replacing the di; scale bar: 0.5 mm, XPL; (d) phl- zone with oriented phl
1220 aggregates, recrystallized dol and anhedral interstitial cal. XPL.

1221 Fig. 11: Concordia diagrams showing U-Pb geochronology results for zircons from
1222 felsic and mafic apophyses and respective CL images of representative zircon grains of

each sample (a) A2 felsic apophysis magmatic age, hbl-bt granodiorite sample DB-G2Z, location in outcrop shown in Fig. 3b. (b) A1 mafic apophysis inherited zircon ages, sample DB-G1Z, location in outcrop shown in Fig. 3b; and (c) Magmatic and inherited zircon grains from A2 felsic apophysis, sample DB-G2Z. (d) Inherited zircon populations from A1 mafic apophysis, sample DB-G1Z. Laser ablation spot analyses are identified by number (refer to tables S1-S2 for results) on the zircon CL images in (c)-(d).

Fig. 12: Tera-Wasserburg diagrams showing U-Pb isotope analysis of (a) titanite and (b-c) apatite from A1 mafic apophyses.

Fig. 13: Calculated Schreinemarkers diagrams showing the effect of temperature, X_{CO_2} and SiO_2 activity on relevant diopside and forsterite forming reactions and stability fields and possible paths for the different interpretations described in the text. Arrows 1 to 4 represent the changes in effective fluid flux interpretation where 1 and 2 refer to variable X_{CO_2} at relatively high a_{SiO_2} , arrows 3 and 4 refer to the changes in a_{SiO_2} and gray arrows 5 and 6 indicate a unlikely but possible cooling path at constant flux at low X_{CO_2} and a_{SiO_2} . S1 = scenario 1; S2 = scenario 2.

Fig. 14: Schematic evolution model for metasomatic stages associated to the intrusion of the syntectonic CSGC. (a) A1 mafic and felsic apophyses intrusion into parallel to marble foliation S_1 ; estimate age between 600 and 580 Ma, related to extensional regime (b) Metasomatic stage 1: shift to a transpressional regime resulting in folding of the marbles and A1 apophyses; intrusion of A2 felsic apophyses; metamorphism of A1 mafic apophyses; formation of structurally-controlled diopside and forsterite skarns within dolomitic marbles by infiltration of SiO_2 -bearing aqueous fluids released from cooling felsic apophyses at c. 578 Ma. (c) Metasomatic stage 2: final assembly of the magmatic complex after decrease in magmatic activity; cooling and brittle fracturing of the complex and associated wallrocks; infiltration of aqueous fluids released from final granitic bodies and pegmatites causing serpentinization of skarn assemblages, chloritization of biotite in felsic

1249 and mafic apophyses and formation of calcite-chlorite-sulphide hydrothermal veins and
1250 breccias near subvertical faults at c. 557 Ma.

1251 Fig. 15: Schematic sketch showing the evolution of the decisive parameters
1252 temperature, $X(\text{CO}_2)$ and SiO_2 activity for the different interpretations of the skarn
1253 sequence. The right-side diagram illustrates the development of the fluid flux over time. S1
1254 = Scenario 1; S2 = Scenario 2.